Article

Intrinsic dysfunction in muscle stem cells lacking dystrophin begins during secondary myogenesis

Marie E. Esper [1,2], Alexander Y. T. Lin[1,2], Dallas Bennett[1] & Michael A. Rudnicki [1,2,3]

Loss of dystrophin causes Duchenne Muscular Dystrophy (DMD), a neuro-muscular disease characterized by muscle fragility and muscle stem cell (MuSC) impairment. Conventional understanding is that DMD manifests after birth from cumulative muscle damage. Here, examination of *mdx* mouse embryos lacking dystrophin reveals no impairment of the primary myogenic program. By contrast, histological and single cell RNA-sequencing analysis during secondary myogenesis uncovers an increase in the proportion of fetal (f) MuSCs and a marked reduction in myogenic progenitors and myocytes, leading to fewer smaller-caliber myofibers. Wild type fMuSCs express full-length dystrophin that interacts with MARK2, whereas *mdx* fMuSCs down-regulate MARK2 and NUMB, exhibiting reduced PARD3 polarization. Strikingly, deletion of the Numb Associated Kinase, AAK1, rescues polarization of NUMB and myogenic progenitor generation in *mdx* fetal muscle. Together, our results elucidate an acute disease pathology during DMD fetal development and the potential for therapeutic intervention by targeting AAK1.

No cure exists for Duchenne Muscular Dystrophy (DMD), a fatal muscle degenerative disease caused by loss-of-function mutations in the dystrophin gene (*DMD*). *DMD* contains seven tissue-specific promoters, with loss of the full-length 427 kDa muscle isoform driving DMD pathology[1,2]. In post-natal muscle, full-length dystrophin is expressed in myofibers and muscle stem cells (MuSCs), where it plays important structural and signaling roles through the dystrophin-associated glycoprotein complex (DGC)[3,4]. Without dystrophin, the DGC does not assemble and is unable to tether the extracellular matrix (ECM) to the intracellular actin cytoskeleton through the sarcolemmal protein dystroglycan. This results in two consequences: myofiber fragility and disrupted MuSC function[4–8].

Dystrophin and DGC components are expressed in activated MuSCs where dystrophin interacts with the polarity kinase MARK2 to establish MuSC polarity[4,7,8]. Without dystrophin, MARK2 is down-regulated, PARD3 polarity is disrupted, and MuSCs undergo fewer

asymmetric divisions, producing fewer progenitor cells[4,8]. Interestingly, despite reports of full-length *Dmd* expression during early murine and human myotome development, the effect of dystrophin deficiency on embryonic myogenesis has remained unclear[9,10].

DMD is conventionally thought to manifest at 3–5 years of age when the accumulation of contraction-induced muscle injuries leads to gross motor delays, abnormal gait, frequent falls and difficulty standing[11]. However, despite DMD patients appearing asymptomatic at birth, several studies suggest that the etiology of DMD begins *in utero*. For instance, studies describe disrupted muscle development in 12-week fetal human muscle[12], and in the muscle of dystrophin-deficient animal models, including the neonatal dystrophic golden retriever (*GRMD*), the *mdx* mouse fetus and neonate and the *sapje* zebrafish embryo[8,13–15]. Further, transcriptional dysregulation occurs in DMD patient muscle before 2 years of age and in disease modeling of myogenesis using patient-derived induced pluripotent stem cell

[1]Sprott Centre for Stem Cell Research, Regenerative Medicine Program, Ottawa Hospital Research Institute, Ottawa, ON, Canada. [2]Department of Cellular and Molecular Medicine, Faculty of Medicine, University of Ottawa, Ottawa, ON, Canada. [3]Department of Medicine, Faculty of Medicine, University of Ottawa, Ottawa, ON, Canada. ✉e-mail: mrudnicki@ohri.ca

(hiPSC)[16–18]. Another recent study demonstrated that during in vitro somitogenesis, hiPSCs diverge to an alternative branch of myogenic trajectory, and these cells have dysregulation of gap junction genes[18]. Considering the recently appreciated role of dystrophin in postnatal MuSCs, we questioned whether the absence of dystrophin in embryonic or fetal myogenic progenitor cells contributes to developmental abnormalities in the dystrophin-deficient embryo.

Using the *mdx* mouse model of DMD[19], our in-depth characterization of primary and secondary myogenesis demonstrates that DMD is an intrinsic MuSC disease that begins *in utero*. Dystrophin regulates fMuSC polarity during secondary myogenesis, and its absence leads to fMuSC expansion and reduced numbers of myogenic progenitor cells before inflammation and muscle necrosis[19]. We also find that targeting the NUMB antagonist AAK1 rescues secondary myogenesis. Together, our results suggest that earlier therapeutic intervention may be warranted.

Results

Primary myogenesis is not affected by dystrophin deficiency

To investigate the significance of dystrophin deficiency during primary myogenesis, comparative analysis between C57BL/10ScSnJ wild type (WT) and *mdx* embryos was performed at E10.5, shortly after commitment of the first myogenic cells in the somite. Following segmentation, the somite is partitioned into the ventral sclerotome and the dorsal dermomyotome, a multipotent structures that give rise to primary myofibers of the myotome (Supplementary Fig. 1a)[20]. Staging of E10.5 WT and *mdx* embryos using somite enumeration and the Embryonic Mouse Ontogenetic Staging System (eMOSS)[21] revealed a subtle difference in staging between genotypes. On average, WT embryos had 1.2 additional somite pairs and were staged 1.9 h ahead of *mdx* embryos (Supplementary Fig. 1b, c), consistent with the mean segmentation rate of one somite pair every two hours in mice[22].

To directly evaluate myogenic cell commitment, we stage-matched WT and *mdx* E10.5 embryos by somite number and eMOSS age before whole mount (Supplementary Fig. 1d,e) and cross-section histological analysis (Supplementary Fig. 1f, g). In both analyses, the number of PAX7^{+} and MYOG^{+} cells in the dermomyotome and myotome was similar between genotypes at the forelimb bud level (Supplementary Fig. 1e, g). Similarly, the proportion of MYOG^{+} cells in the entire PAX7^{+} and MYOG[+] cell population, as determined by whole mount and cross-section analysis combined, was not significantly changed (Supplementary Fig. 1h). We also observed no difference in the number of PAX3^{+} cells in the E10.5 dermomyotome (Supplementary Fig. 1f, g).

Promoters on exon 1 of *Dmd* initiate transcription of isoforms encoding the full-length dystrophin protein, which is required for MARK2-mediated cell polarity and is universally lost in null DMD patients and *mdx* mice. Internal promoters, located 3′ of the *mdx* mouse mutation, generate N-terminal truncated isoforms[1,4]. Western blot analysis of the E10.5 trunk and limbs using antibodies specific to repeats 8–9 and the C-terminus of dystrophin identified short but not full-length dystrophin (Supplementary Fig. 2a). Interestingly, full-length utrophin (UTRN) and β-dystroglycan (β-DG) were expressed at the dermomyotome basal lamina, demarcated by laminin staining (Supplementary Fig. 2b–d). Thus, dystrophin does not appear to play a role in regulating primary myogenesis.

Delayed myofiber development in *mdx* fetal muscle

To assess the consequence of dystrophin deficiency during secondary myogenesis, cross-sectional sarcolemmal and ECM staining of WT and *mdx* fetal hindlimbs was performed at E14.5 and E17.5. We also examined muscles collected from WT and *mdx* fetuses crossed with *Myf5-Cre* and *ROSA-nTnG* transgenic alleles. In this model, primitive fMuSC are nuclear tdTomato-positive (tdT[+]) until *Myf5-Cre* expression permanently induces a switch to nuclear EGFP (GFP[+]), which marks cells primed for myogenesis, progenitors, and myonuclei (Fig. 1a). *Myf5Cre*-

negative MuSCs, observed in developing and adult muscle, have increased self-renewal and regenerative ability and are the cells that give rise to *Myf5Cre*-positive cells following asymmetric cell division[23].

At the beginning of secondary myogenesis, laminin staining of the WT and *mdx* E14.5 *extensor digitorum longus* (EDL) revealed reduced expression in the *mdx* fetus. While WT myofibers were surrounded by continuous laminin-rich matrices, intermittent laminin staining surrounded the *mdx* myofibers (Fig. 1b). The laminin staining area was also reduced in the *mdx* EDL compared to WT muscle (Fig. 1c). Taking advantage of the *Myf5-Cre;RnTnG* transgene, we also observed significantly fewer GFP[+] myogenic nuclei in the *mdx* EDL and *tibialis anterior* (TA) at E14.5 (Fig. 1b, d).
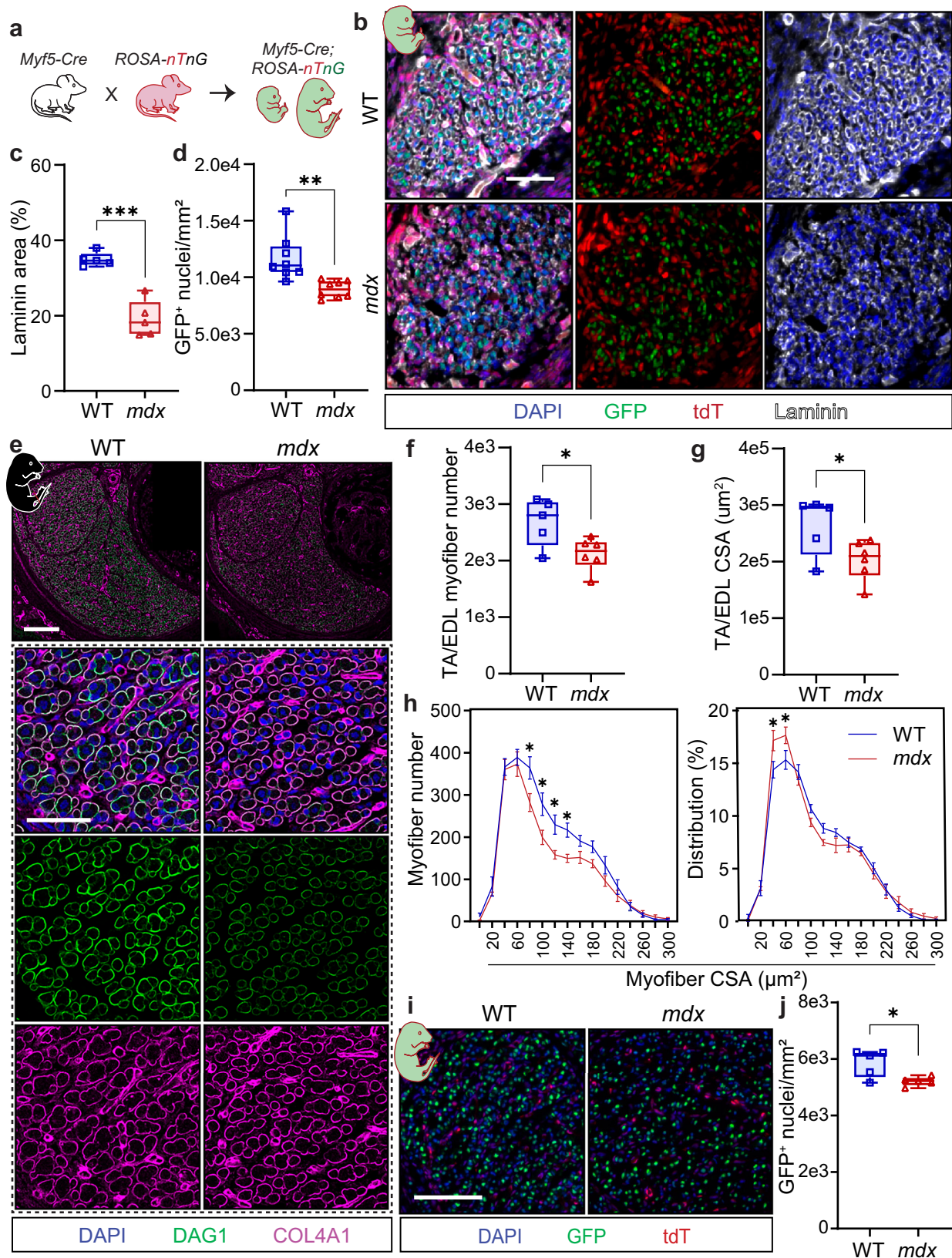
COL4A1 staining showed a continuous ECM surrounding both WT and mdx myofibers by E17.5. (Fig. 1e). However, sarcolemmal DAG1-staining of the E17.5 TA and EDL demonstrated fewer myofibers and reduced total cross-section area (CSA) in *mdx* muscle (Fig. 1e–g). Moreover, the distribution of TA and EDL myofiber area shifted, with a greater proportion of small E17.5 *mdx* myofibers compared to age-matched WT muscle (Fig. 1h). DAG1 expression appeared downregulated in fetal *mdx* hindlimb muscle, as previously observed in postnatal *mdx* muscle (Fig. 1e)[24]. Using COL4A1 staining, we observed decreased myofiber number and CSA in *mdx* fetal EDL cross-sections (Fig. 1e, Supplementary Fig. 3a–c).

Consistent with findings at the beginning of secondary myogenesis, we also observed significantly fewer GFP[+] myogenic nuclei in the *mdx* EDL and TA at E17.5 using the *Myf5-Cre;RnTnG* reporter (Fig. 1i, j). Finally, *mdx* fetal muscle was less dense at E17.5 than WT muscle, as demonstrated by the decreased number of myofibers per mm^2 in the EDL and TA (Fig. 1e, Supplementary Fig. 3d, e), and the increased ratio of ECM relative to myofiber area (Supplementary Fig. 3f). These results align with studies in *mdx* neonates, where myofibers are hypotrophic with fewer myonuclei compared to WT muscle until approximately three weeks of age[25]. Similarly, our myofiber morphology findings are consistent with the discovery that human fetal muscle has reduced myofiber density and size[12].

Considering the subtle staging difference at E10.5 and the absence of a myofiber basal lamina during primary myogenesis[26], we questioned whether the altered laminin staining and reduced myogenic nuclei in *mdx* muscle reflected a delayed transition from primary to secondary myogenesis. NFIX transcriptionally regulates this transition and is upregulated in fetal myogenic cells[27]. RT-qPCR analysis revealed that *Nfix* was expressed at similar levels in GFP^{+} cells isolated from WT and *mdx:Pax7-nGFP* E14.5 limbs (Supplementary Fig. 4a). Comparable numbers of MYH7^{+} primary myofibers were also enumerated on WT and *mdx* E17.5 EDL and TA cross-sections (Supplementary Fig. 4b, c). Therefore, the difference in myofiber morphology observed in *mdx* fetal muscle is likely not due to developmental delays before secondary myogenesis.

Fewer myogenic cells in *mdx* fetal muscle

In adult *mdx* muscle, fewer asymmetric MuSC divisions occur in the absence of dystrophin, leading to the reduced generation of progenitor cells, and hence fewer MYOG-expressing myocytes[4,8]. To assess whether perturbations in fetal myofiber development correlated with a reduction in the number of progenitors, we enumerated the number of PAX7^{+} and MYOG^{+} cells on TA and EDL cross-sections at E14.5 and E17.5 (Fig. 2a, b). The total number of myogenic cells, including PAX7^{+} and MYOG^{+} cells, was reduced at both time points. MYOG^{+} cells were specifically decreased by 36% and 28% at E14.5 and E17.5, respectively (Fig. 2c, d). To account for the global reduction in myogenic cells, we assessed the proportion of MYOG^{+} cells in the entire PAX7^{+} and MYOG[+] population. Interestingly, the proportion of MYOG^{+} cells was reduced at both time points, but more profoundly at E17.5 (Fig. 2e). Our findings are consistent with previously reported decreases in PAX7 expression in *mdx* fetal muscle[15], and reductions in MYOG^{+} cells in neonatal

muscle[8]. Because fMuSCs and progenitors express PAX7, we next questioned whether the diminished number of PAX7^{+} cells arose from changes in *mdx* fMuSCs proliferation or the generation of fewer progenitor cells.

The expression of *Myf5* is a metric of MuSC myogenic specification upstream of MYOG[23,28]. Using the *Myf5-Cre* and *ROSA-nTnG* transgenic lines bred into the WT and *mdx* background, we quantified the number of PAX7^{+} cells that have never expressed *Myf5-Cre* at E14.5 and E17.5 (Fig. 3a, b). We observed fewer PAX7^{+} tdT^{+} cells at E14.5, and a 3.5-fold increase in PAX7^{+} tdT[+] at E17.5 (Fig. 3c). Taking into consideration the decrease in total PAX7^{+} cells that was more pronounced at E14.5, we quantified the proportion of total PAX7^{+} cells that express

Fig. 1 | Abnormal *mdx* myofiber formation during secondary myogenesis.
a Schematic of *Myf5-Cre* and *ROSA-nTnG* breeding pairs used to obtain embryos for analysis of fetal MuSC commitment. Nuclei are tdTomato-positive (tdT⁺) until *Myf5-Cre* expression induces recombination of the *ROSA* allele and EGFP (GFP⁺) expression. **b** Representative immunofluorescence images of E14.5 *extensor digitorum longus* (EDL) from wild-type (WT) and *mdx:Myf5-Cre;ROSA-nTnG* fetuses with DAPI counterstain (blue), endogenous GFP (green) and tdT (red), and laminin staining (white). Scale bar, 50 μm. **c** Percent of EDL area stained with anti-laminin. For **b**, **c**, n = 5 per genotype. **d** Number of GFP⁺ nuclei normalized to mm² enumerated on WT and *mdx Myf5-Cre;R-nTnG* hindlimb TA and EDL cross-sections at E14.5. n = 8 per genotype. **e** Example immunofluorescence images of entire wild type (WT) and *mdx extensor digitorum longus* (EDL) and *tibialis anterior* (TA) at E17.5 (top; scale bar, 100 μm) and magnified insets (bottom; scale is 50 μm). DAPI counterstain (blue), DAG1 (green) denotes sarcolemma, and COL4A1 (magenta) marks the

extracellular matrix. Total TA and EDL myofibers number (**f**) and myofiber cross-section area (CSA; μm²) (**g**) at E17.5 based on DAG1 staining. **h** Size distribution of E17.5 myofibers using myofiber CSA (μm²) based on DAG1 staining. Left is number of fibers and right is normalized size distribution. Data presented as mean values ± SEM. For **e**–**h**, n = 5 for WT and n = 6 for *mdx*. **i** Representative immunofluorescence images of E17.5 EDL cross-section from WT and *mdx:Myf5-Cre;ROSA-nTnG* fetuses expressing endogenous GFP (green) and tdT (red), counterstained with DAPI (blue). Scale bar, 100 μm. **j** Number of GFP⁺ nuclei normalized to mm² enumerated on WT and *mdx Myf5-Cre;R-nTnG* hindlimb TA and EDL cross-sections at E17.5. For **i**, **j**, n = 5 per genotype. Statistical analysis performed using two-tailed unpaired *t*tests, except for **j** where a two-way ANOVA followed by Sidak's post hoc test with adjustment for multiple comparisons was performed (*$p < 0.05$, ** $p < 0.01$, *** $p < 0.001$). Exact *p*values included in the **Source Data**. Box plots show the median, the 25th and 75th percentiles, and whiskers are the minimum and maximum values.
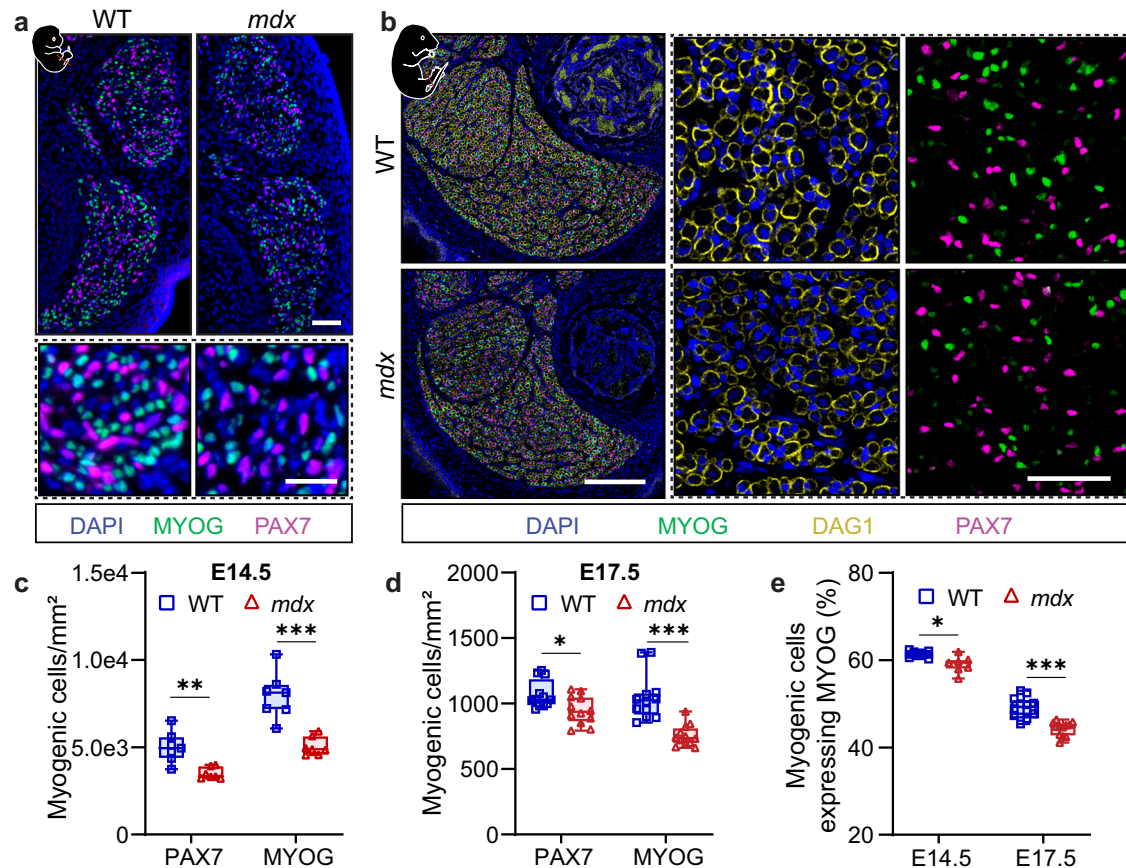

Fig. 2 | Fewer committed myogenic cells in E17.5 *mdx* muscles. a Representative immunofluorescence images of wild-type (WT) and *mdx tibialis anterior* (TA) and *extensor digitorum longus* (EDL) muscles from hindlimb transverse sections at embryonic day (E) 14.5 (top; scale bar, 50 μm) and magnified inset (bottom; scale bar, 25 μm). MYOG (green) denotes differentiating progenitor cells, and PAX7 (magenta) labels fetal MuSCs. **b** Immunofluorescence image examples of WT and *mdx* TA and EDL from hindlimb transverse sections at E17.5 (scale bar, 200 μm) and magnified inset (scale bar, 50 μm). MYOG (green) denotes differentiating progenitor cells, DAG1 (yellow) marks fetal sarcolemma, and PAX7 (magenta) labels

fetal MuSCs. Enumeration of myogenic cells expressing either PAX7 or MYOG at E14.5 (**c**) and E17.5 (**d**) and normalized to mm². **e** Proportion of MYOG⁺ cells relative to entire PAX7⁺ and MYOG⁺ cell population at E14.5. and E17.5. n = 7 per genotype at E14.5, and n = 12 per genotype at E17.5. Box plots show the median, the 25th and 75th percentiles, and whiskers are the minimum and maximum values. Data analyzed using two-way ANOVA corrected for multiple comparisons using Sidak's post hoc test where *$p < 0.05$, **$p < 0.01$, and ***$p < 0.001$. Exact *p*values included in the **Source Data**.

tdT. No change in the relative proportion of PAX7⁺ tdT⁺ cells was observed at E14.5, while a notable increase in the proportion of uncommitted PAX7⁺ tdT⁺ cells occurred at E17.5 (Fig. 3d). This suggests that the number of uncommitted fMuSCs is expanded in *mdx* E17.5 fetal muscle during secondary myogenesis.

Increased fMuSC and fewer progenitors in *mdx* fetal muscle
To investigate myogenic cell state and gene expression profiles of fMuSCs in dystrophin-deficient fetal muscle, we isolated GFP⁺ cells in

biological duplicates from the limbs of WT and *mdx:Pax7-nGFP* embryos at E17.5 for single cell RNA-seq (scRNA-seq) (Supplementary Fig. 5a). Residual GFP allowed us to study the progression from uncommitted fMuSCs to terminally differentiated myocytes. Following quality control, filtering and dimensional reduction of the combined libraries, 7 clusters containing 21,734 WT and 25,064 *mdx* cells were identified and annotated based on differential gene expression testing (Supplementary Fig. 6a, Supplementary Data 1). Five clusters, which comprised 95% of the libraries, regardless of genotype,
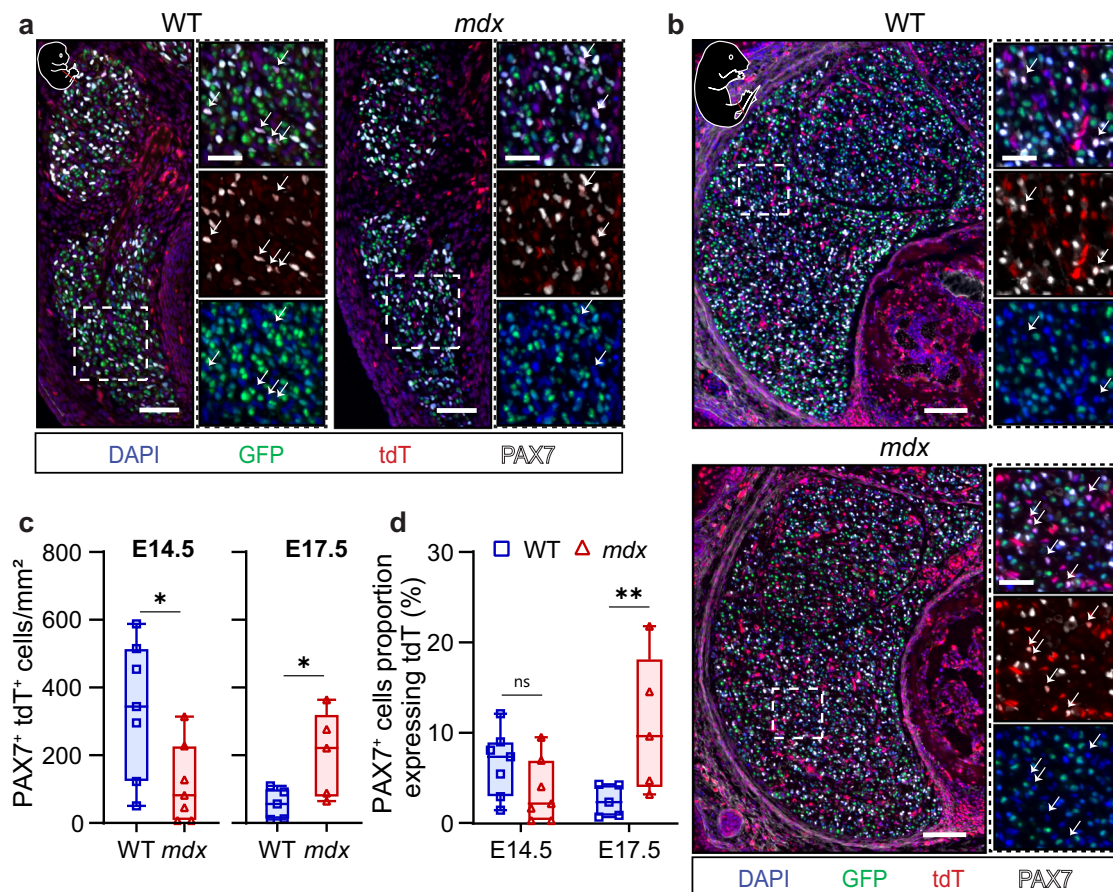
Fig. 3 | Increased numbers of uncommitted fetal MuSCs in *mdx* muscle.
Representative images of the *tibialis anterior* (TA) and *extensor digitorum longus* (EDL) muscles from WT and *mdx Myf5-Cre;R-nTnG* hindlimb cross-sections at E14.5 (**a**) and E17.5 (**b**). Nuclei express endogenous tdTomato (tdT+; red) or EGFP (GFP+; green), and PAX7 (white) marks fetal (f) MuSCs. In **a**, the scale bar is 50 μm and 25 μm (insets). In **b**, scale bars are 100 μm and 25 μm (insets). White arrows denote PAX7+ tdT+ cells. **c** Enumeration of PAX7+ tdT+ myogenic cells normalized to mm² at E14.5 and E17.5. Statistical analysis performed using two-tailed unpaired *t* tests ($*$ < 0.05). **d** Proportion of total PAX7+ cells that express tdT at E14.5 and E17.5 from WT and *mdx Myf5-Cre;R-nTnG* hindlimb TA and EDL cross-sections. Data analyzed using a two-way ANOVA followed by Sidak's post hoc test with adjustment for multiple comparisons ($** p < 0.01$, ns = not significant). Exact *p*values included in the **Source Data**. *n* = 7 per genotype at E14.5 and *n* = 5 per genotype at E17.5. Box plots show the median, the 25th and 75th percentiles, and whiskers are the minimum and maximum values with adjustment for multiple comparisons.

represented the myogenic continuum, from undifferentiated fMuSCs to post-mitotic myocytes, and were the focus of further analyses (Supplementary Fig. 6b, c).

To minimize the effect of cell cycle on clustering, mitosis scores were assigned using Seurat's CellCycleScoring function, then the S and G2/M phase scores were regressed using scTransform. Dimensional reduction and re-clustering identified 11 myogenic cell clusters with unique features (Supplementary Fig. 6c, Supplementary Data 2). The clusters were ordered hierarchically based on decreasing *Notch3* expression[23], concurrent emergence of *Hes6*[29], and the general sequence of MRF and differentiation marker expression (Supplementary Fig. 6d, e, Supplementary Data 2).

fMuSC clusters were generally characterized by elevated *Pax7* expression, the absence of *Myog*, and the expression of Notch and ECM genes that are linked to post-natal MuSC quiescence and activation (Supplementary Fig. 6d, e, Supplementary Data 2)[29–31]. 'fMuSCs 1' and 'fMuSCs2' were enriched in oxidative phosphorylation genes and expressed elevated *Pax7*, *Notch3*, *Col4a1*, *Lama2*, and *Itgb1*, and negligible *Myf5* and *Myod1*. Based on the elevated expression of quiescent MuSC niche genes and the metabolic gene signature, we theorized fMuSCs 1 and 2 are fMuSCs residing in the nascent fetal myofiber niche and contributing to its formation. 'fMuSCs 3' and 'fMuSCs4' expressed *Myf5* but not *Myod1*, while 'fMuSC 5' and 'fMuSCs 6' expressed both MRFs. All four *Myf5*-expressing fMuSC clusters shared increased

expression of activation related genes such as the AP1 transcription factors *Junb* and *Fos*, the ECM genes *Lama5* and *Col5a1*, and the proliferation and activation-related Notch genes *Notch1*, *Notch2*, *Notch3*, *Hes1*, and *Hes6*[31–35]. 'fMuSCs 7' shared similarities to the four 'activated' clusters, but with reduced expression of MuSC and activation-related genes including *Pax7*, *Notch2*, *Notch3*, *Lama2*, *Lama5*, and *Col5a1*, and elevated expression of ribosomal and cell cycle genes such as *Ccnd1*, *Ccnb2*, and *Pttg1*, suggesting this was a committed fMuSC cluster.

Interestingly, we observed striking fMuSC heterogeneity. The fMuSCs 4 cluster expressed elevated genes related to TGF-β and MAPK signaling, focal adhesions, and smooth muscle, including *Igf1*, *Ltbp1*, *Rgma*, *Pitx2*, *Tgfb2*, *Met*, *Itga1*, *Nppc*, and *Cav1*. fMuSCs 2 and fMuSCs 5 expressed elevated *Nrg1*, *Col19a1*, *Adgrb3*, *Fgf12*, *Slit2*, *Bmpr1b*, *Meis1*, and *Nell1*, genes linked to BMP signaling and neurogenesis. Finally, fMuSCs 6 were enriched for the interleukin 1 receptor family gene *Il1rapl2*, in addition to *Eya2*, *Sfrp2*, *Exoc6*, *Fat3*, *Nckap5*, and *Zic1* (Supplementary Fig. 6d, e, Supplementary Data 2).

Four progenitor cell clusters were identified in the WT and *mdx* libraries. 'Progenitors' expressed *Pax7*, *Myf5*, *Myod1*, *Mki67*, and low levels of *Myog*, while 'Committed Progenitors' expressed very little *Pax7*, and elevated *Myod1*, *Myog*, and *Mymx*. Two distinctly different myocyte clusters were also observed. The larger 'Myocytes' cluster expressed dogmatic differentiation markers such as *Myog*, *Mymx*, and *Acta1*, the cell cycle inhibitor *Cdkn1a*, and very little *Dmd*. The smaller
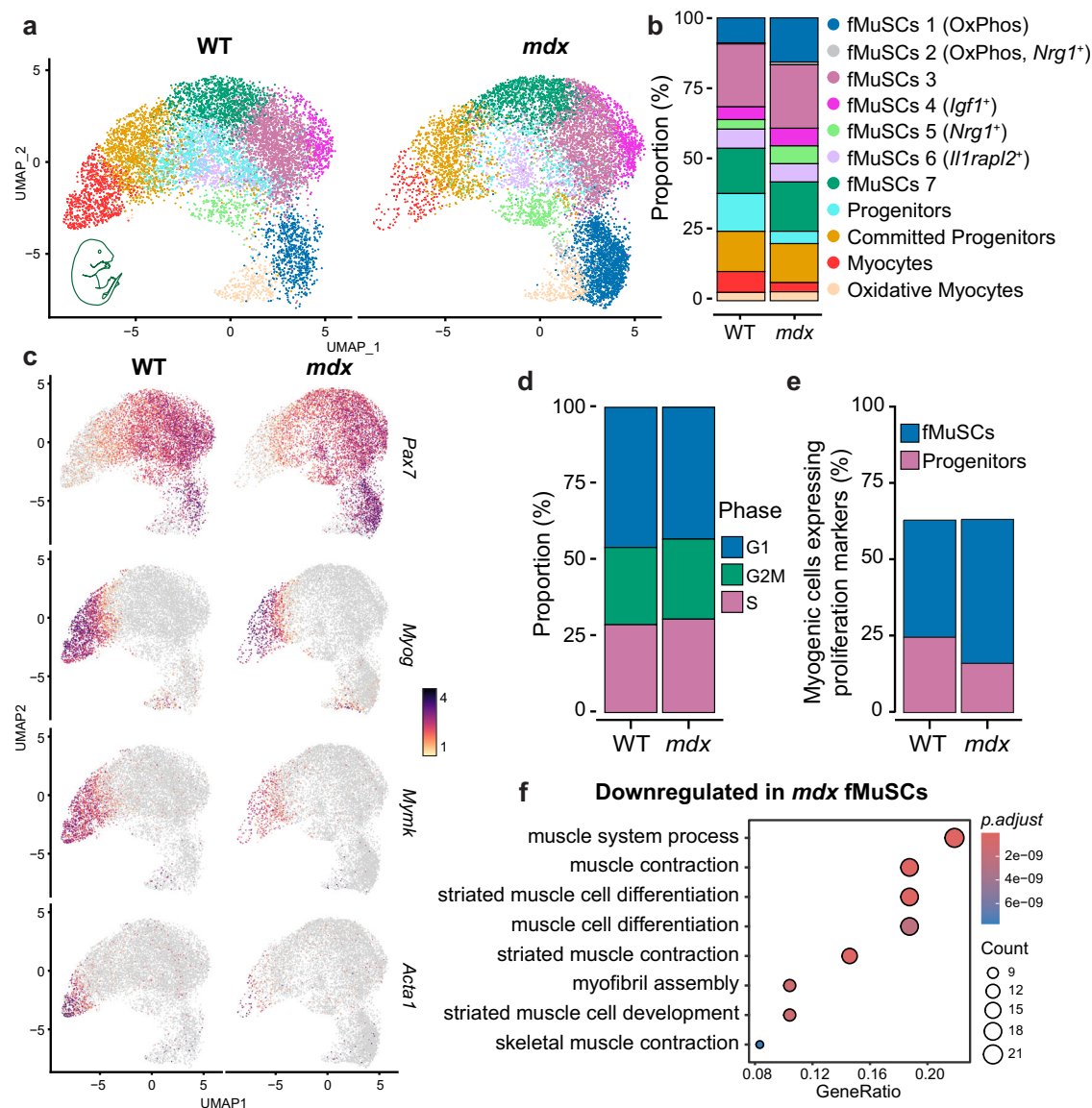
Fig. 4 | Single cell RNA-sequencing uncovers reduced numbers of *mdx* progenitors. a Uniform manifold approximation and projection (UMAP) visualization of wild type (WT) and *mdx* myogenic cells isolated from *Pax7-nGFP* E17.5 fetal limbs for single cell RNA-sequencing libraries. 9000 cells are illustrated per genotype. **b** Bar plot illustrating library cluster proportions for WT and *mdx* myogenic libraries. *n* = 2 biological replicates. For **a**, **b**, clusters are schematically depicted in hierarchical order from fetal (f) MuSCs to myocytes and grouped by genotype. **c** Feature plots illustrating the expression of *Pax7* and commitment markers *Myog*, *Mymk* and *Acta1*. **d** WT and *mdx* library proportions split by cell cycle phase, as

determined by Seurat's cell cycle scoring. **e** Proportion of library expressing proliferation markers (*Cenpa*, *Mki67* or *Cdk1*), split by fMuSC and progenitor cell identity. **f** Gene ontology terms enriched in genes significantly downregulated in *mdx* compared to WT pseudobulked myogenic cell libraries, as identified by Seurat's FindMarkers function with default Wilcoxon test. GO term enrichment was performed using enrichGO with default parameters, including the hypergeometric test and Benjamini-Hochberg correction for multiple testing. For **d**–**f**, *n* = 2 biological replicates. Exact *p*values are included in Supplementary Data 2–4. See also Supplementary Fig. 6.

'Oxidative Myocyte' cluster expressed elevated OxPhos genes, *Myog*, and *Utrn*. The oxidative myocyte cluster also shared upregulated genes with the two *Nrg1*⁺ fMuCS clusters, including *Bmpr1b*, and *Col19a1* (Supplementary Fig. 6d, e, Supplementary Data 2).

Cells in the WT and *mdx* libraries clustered together without bioinformatic integration (Fig. 4a). However, as seen by histological analysis, *Pax7*⁺ fMuCSs clusters were over-represented in the *mdx* libraries (Fig. 4a, b). The fMuSC clusters constituted 62% and 76% of the WT and *mdx* libraries, respectively, while the *Myog*⁺ progenitor cell clusters accounted for the remaining 38% and 24% (Fig. 4b). Interestingly, the *Myf5*-low fMuSCs 1 cluster represented 12% of the WT library and 20% of the *mdx* libraries, which corroborates our findings using the *Myf5-Cre;ROSA-nTnG* allele, where we observed an expansion of the uncommitted fMuSC population at E17.5 (Fig. 3d). Comparing WT and

mdx myogenic cells using feature plots further illustrates the over-representation of *Pax7*⁺ cells, and the reduced expression of the commitment markers *Myog*, *Mymk*, and *Acta1* (Fig. 4c).

Cell cycle scoring indicated that slightly more than half of both WT and *mdx* libraries were in G2M or S phase, with no notable differences between genotypes (Fig. 4d). However, the proportion of *Mki67*⁺ progenitors was drastically reduced in the *mdx* libraries (Fig. 4a, b), which should account for a large portion of proliferating cells. We therefore examined the number of cells expressing the proliferation markers *Cenpa*, *Mki67*, and *Cdk1* and categorized these into fMuSC or progenitor clusters. As observed by cell cycle scoring, the overall number of proliferating cells was nearly identical (64%) between genotypes. However, proliferating fMuSCs accounted for 39% of the WT and 48% of the *mdx* libraries, whereas proliferating progenitors comprised 25% of the WT

and 16% of the *mdx* libraries, respectively (Fig. 4d). This corresponded to a 22% increase in proliferating fMuSCs concomitant with a 34% reduction in proliferating progenitors in the *mdx* libraries compared to WT. The differences observed in the transcriptomic data support the finding that *mdx* fMuSCs have a diminished capacity to generate progenitor cells.

Next, we performed differential gene expression testing on the pseudobulked WT and *mdx* libraries and found 1604 downregulated and 580 upregulated genes in the *mdx* libraries (Supplementary Data 3). Further corroborating the reduced number of *mdx* progenitor cells, we observed downregulated genes related to muscle commitment, including *Actc1*, *Myog*, *Mymx*, *Tnnt2*, and *Acta1*, in addition to genes such as *Camk1d*, *Lars2*, *Erh*, *Cdv3*, *Eno1*, *Igf2*, and *Ddx6* in the entire libraries. Gene ontology (GO) analysis of the downregulated genes similarly highlighted terms such as 'muscle system process,' 'muscle contraction,' and 'muscle cell differentiation' (Fig. 4f, Supplementary Data 4).

In the pseudobulked *mdx* libraries, upregulated genes included *Hes1*, *mt-Nd2*, and *Igf1r*, in addition to genes related to TGF-β signaling (*Bmpr1b*, *Id1*, *Thsd4*, and *Ltbp1*), and genes associated with the fMuSCs 5 cluster (*Meis1*, *Fgf12*, *Col19a1*, *Slit2*, *Robo2*, and *Nrg1*). *Prkca*, a calcium-dependent protein kinase C, was also elevated, which was previously observed in fetal human DMD muscle (Supplementary Data 3)[12]. Given that Notch and TGF-β signaling inhibit myogenic cell differentiation, this provides further evidence of reduced numbers of differentiation-competent *mdx* myogenic cells[32,36,37]. Unlike adult myogenic cells analyzed by scRNA-seq[8], the aberrant proportions of fMuSCs and progenitor cells occurred without inflammatory response gene upregulation. This supports the notion that intrinsic deficits, rather than the inflammatory microenvironment alone, contribute to MuSC polarity dysfunction in *mdx* postnatal muscle.

Notably, fMuSC clusters were enriched for adhesion, ECM, and DGC genes, requirements for dystrophin-mediated cell polarity. These included collagens, laminins, cadherins, integrins, immunoglobulin adhesion molecules, syndecans, and fibronectin (Supplementary Fig. 6d, 7, Supplementary Data 3). DGC genes expressed in the fMuSC clusters included *Dag1*, *Sgce*, *Dtnb*, *Sspn*, and *Dmd*. Interestingly, the PAR complex genes *Mark2* and *Pard6g* were also enriched in the fMuSC clusters, while *Pard3* was ubiquitously expressed (Supplementary Fig. 7).

Dystrophin and MARK2 are expressed and polarized in fMuSCs

MARK2 interacts with dystrophin (DMD) at repeats 8–9 of the full-length 427 kDa protein, which is necessary for PAR complex-mediated MuSC polarity, asymmetric division and the generation of myogenic progenitors[4,8,38]. To assess whether full-length dystrophin was expressed in fMuSCs, we isolated GFP⁺ cells from *Pax7-nGFP* limb muscles at multiple time points, then performed RNAscope and immunostaining using probes and antibodies specific to the full-length isoform. MuSCs isolated from adult *Pax7-nGFP* mouse hindlimb muscles were included as controls (Fig. 5a, b, Supplementary Fig. 5a).

We observed that 95% of freshly isolated (Fi) MuSCs from healthy adult hindlimb muscle expressed full-length *Dmd* mRNA, which dropped to 31% in activated (A) MuSCs 48 h following cardiotoxin (CTX)-injury (Fig. 5a, c). The drop in dystrophin mRNA aligns with *Dmd* expression data extracted from previously published bulk RNA-seq conducted on postnatal FiMuSC, AMuSCs, primary myoblasts, and 2-day differentiated myotubes[8]. Conversely, DMD protein was not expressed in FiMuSCs, but 25% of AMuSCs were DMD⁺ (Fig. 5b, d)[4]. This suggests that *Dmd* transcript is continuously transcribed in quiescent MuSCs. Interestingly, we also observe elevated relative *Dmd* expression in the OxPhos MuSC clusters, which we predict are fMuSCs taking up or laying down their niche (Supplementary Fig. 6d).

As anticipated, neither full-length dystrophin transcript nor protein were expressed in GFP⁺ cells isolated from E12.5 embryos (Fig. 5a–d). However, full-length RNA and protein were observed in 33% and 13% of GFP⁺ cells, respectively, at E15.5, and in 39% and 13% of

cells at E17.5. At P7, 33% and 19% of neonatal GFP⁺ cells expressed full-length dystrophin RNA and protein, respectively (Fig. 5a–d).

Next, we isolated PAX7⁺ cells from E17.5 WT limbs (Supplementary Fig. 5b) and examined the expression of MARK2 and full-length DMD protein by immunostaining. Approximately 8% of PAX7⁺ cells co-express MARK2 and DMD protein, with a subset exhibiting polarized expression (Fig. 5e). Several polarized fMuSCs displayed uniform PAX7 staining in the cell cytoplasm and bright chromosome staining, suggesting that these cells were entering mitosis. Immunostaining to detect the mitotic marker phospho histone H3 Ser10 (pH3) on FACS-isolated fMuSCs demonstrated that most cells with cytoplasmic PAX7 staining also expressed pH3 (Supplementary Fig. 8).

Dystrophin is required for efficient fMuSC polarization

To assess the interaction of dystrophin and MARK2 in fMuSCs, we isolated WT and *mdx* GFP⁺ cells from *Pax7-nGFP* limb muscles and performed proximity ligation assay (PLA) using antibodies against MARK2 and repeats 8–9 of DMD (Supplementary Fig. 5a). Bright foci were present in WT fMuSCs but absent in *mdx* cells (Fig. 6a–c). To determine whether dystrophin deficiency impacts MARK2 expression, we stained WT and *mdx* GFP⁺ cells for MARK2 (Fig. 6d). As seen in adult MuCSs[4], the number of *mdx* GFP⁺ cells expressing MARK2 was markedly reduced relative to WT cells (Fig. 6e). Further, the overall expression of MARK2 was reduced in GFP⁺ cells isolated from E17.5 *mdx* muscle, demonstrated by reduced mean fluorescence intensity (MFI) (Fig. 6f)[4].

The absence of MARK2-DMD interactions in post-natal MuSCs is associated with the loss of PARD3 polarization, and significantly reduced numbers of asymmetric divisions and progenitor cells[4,8]. To study whether polarity is similarly perturbed in *mdx* fMuSCs, we examined PARD3 polarization in PAX7⁺ fMuSCs isolated from WT and *mdx* fetal limbs at E17.5 (Fig. 6g, Supplementary Fig. 5b). As seen at the RNA level by scRNA-seq, PARD3 was ubiquitously expressed at similar intensities in 96.7% and 97.4% of WT and *mdx* fMuSCs, respectively (Fig. 6g-i). However, the number of PAX7⁺ cells expressing polarized PARD3 was reduced from 62% in WT conditions to 27% in *mdx* cells (Fig. 6j). Thus, though the ability of *mdx* fMuSCs to express PARD3 is not impacted, we find that dystrophin is an important regulator of PARD3 polarization.

Considering the morphological and cellular differences observed in *mdx* fetal muscle at E14.5 and E17.5 compared to age-matched WT muscle, we examined whether fMuSC polarity deficits arise at the onset of secondary myogenesis. Immunostaining of PARD3 on GFP⁺ cells isolated from E14.5 WT and *mdx:Pax7-nGFP* fetal limbs revealed that PARD3 expression was reduced in *mdx* fMuSCs (Supplementary Fig. 9a, b). Further, the proportion of GFP⁺ PARD3⁺ cells with polarized PARD3 expression was also decreased in the absence of dystrophin (Supplementary Fig. 9c). Thus, fMuSC polarity disruptions arise at the onset of secondary myogenesis in the *mdx* fetus.

Notch signaling is dysregulated in *mdx* fMuSCs

The Notch signaling gene *Hes1* was included in the top ten most upregulated genes in the *mdx* fMuSC scRNA-seq libraries by pseudo-bulb differential gene expression analysis, suggesting that Notch signaling is upregulated in dystrophin-deficient fMuSCs (Fig. 7a, b). Interestingly, PARD3 is a positive regulator of Notch signaling that acts through NUMB and NUMBL to promote asymmetric radial glial cell fate[39]. NUMB is an endocytic adaptor protein, a Notch inhibitor, and a cell fate determinant that regulates asymmetric cell divisions through its polarized accumulation[40,41]. In mammalian cells, PARD3-dependent phosphorylation of NUMB by aPKC leads to the asymmetric distribution of NUMB and PARD3/aPKC[39]. Moreover, mammalian NUMB overexpression antagonizes the transactivation of the *Hes1* promoter in a NOTCH1-dependent manner[42]. Given that *mdx* fMuSCs have decreased PARD3 polarization (Fig. 6j) and increased *Hes1* expression,
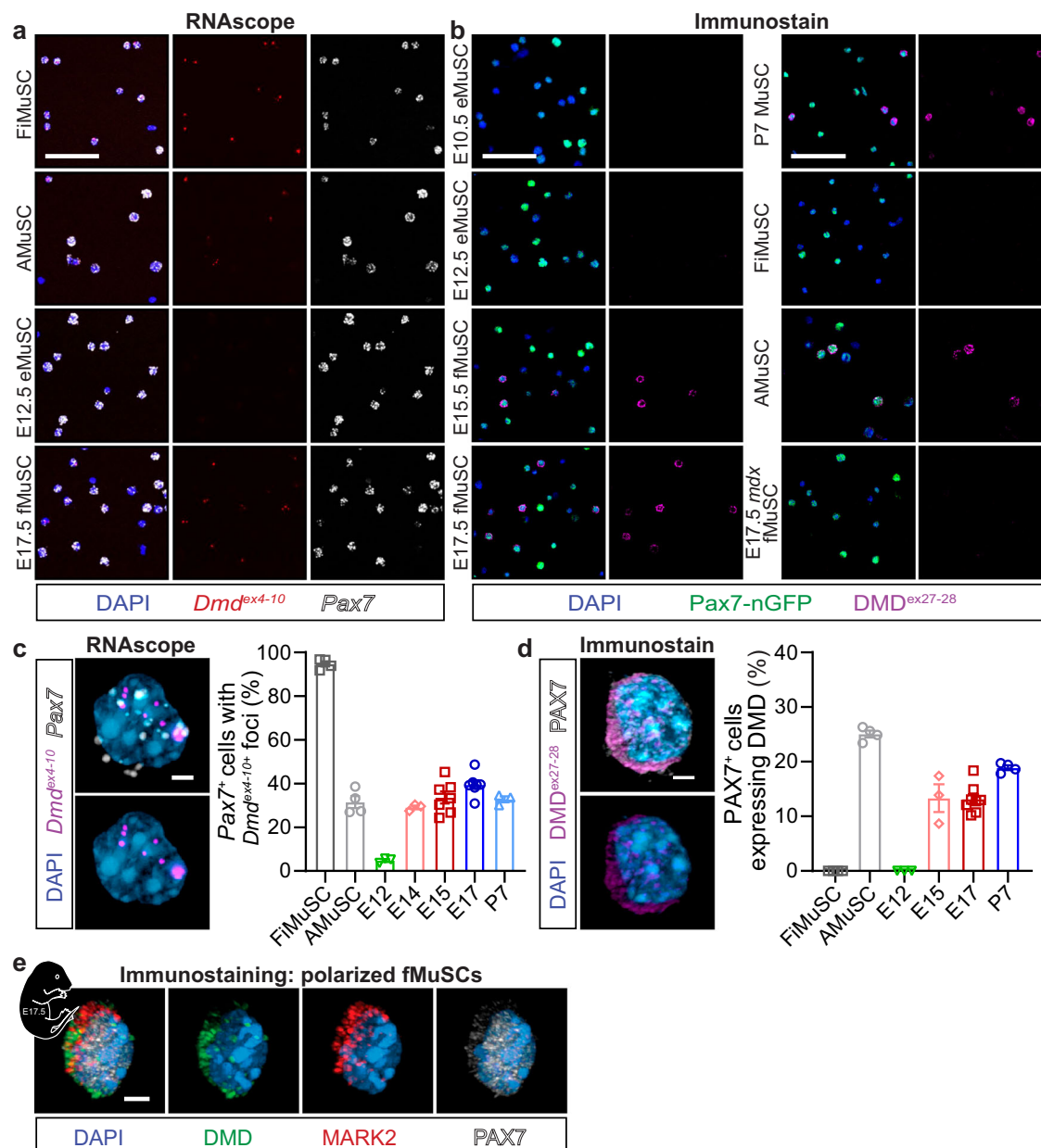
Fig. 5 | Dystrophin and MARK2 are expressed in fetal MuSCs. a Example images of freshly isolated adult MuSCs (fiMuSCs), adult activated MuSCs 48-h following cardiotoxin injury (AMuSCs), embryonic MuSCs (eMuSCs; E12), and fetal MuSCs (fMuSCs; E17) isolated from *Pax7-nGFP* muscle based on GFP expression and treated with RNAscope probes that recognize exons 4–10 of the full-length *Dmd* transcript (*Dmd*$^{ex4-10}$; red) and *Pax7* (white), and counterstained with DAPI (blue). Scale bar, 50 μm. Images are representative of those used for quantification shown in **c**, where each data point corresponds to the number of *Dmd*$^{ex4-10}$-expressing cells per biologic replicate. **b** Immunofluorescent images of GFP$^+$ (green) fiMuSCs, AMuSCs, eMuSCs (E10.5, E12), fMuSCs (E15, E17) and perinatal day 7 (P7) MuSCs isolated from *Pax7-nGFP* mice and stained with an antibody specific to repeats 8 and 9 of the full-length dystrophin protein (DMD$^{ex27/28}$; magenta) and counterstained with DAPI (blue). Scale bar, 50 μm. Images are representative of those used for quantification shown in **d**, where each data point corresponds to the number of DMD$^{ex27/28}$-expressing cells per biological replicate. **c** Left: High resolution image of E17.5 fMuSCs treated with RNAscope probes targeting exons 4–10 of full-length *Dmd* (*Dmd*$^{ex4-10}$; magenta) and *Pax7* (white), and counterstained with DAPI (blue). Scale bar, 2 μm. Right: Quantification of *Pax7*$^+$ myogenic cells expressing *Dmd*$^{ex4-10}$ foci. For **a** and **c**, *n* = 4 FiMuSCs and AMuSCs; *n* = 3 E12, E14 and P7; and *n* = 7 E15.5 and E17.5. **d** Left: Representative image of E17.5 GFP$^+$ (green) fMuSCs stained with an antibody specific to DMD$^{ex27/28}$ (magenta). Scale bar, 2 μm. Right: Quantification of GFP$^+$ myogenic cells expressing DMD$^{ex27/28}$. For **b** and **d**, *n* = 4 FiMuSCs, AMuSCs, P7; *n* = 3 E12, E15; and *n* = 8 E17.5. For c,d, data presented as mean values ± SEM, and statistical analysis not performed. **e** Representative high resolution 3D immunostaining image of E17.5 WT fMuSCs expression polarised dystrophin (DMD; green) and MARK2 (red) protein. Images counterstained with DAPI (blue).

we questioned whether NUMB is downregulated in *mdx* fMuSCs. We therefore analyzed NUMB expression in WT and *mdx* GFP$^+$ cells isolated from *Pax7-nGFP* E17.5 fetal limbs.

The expression of *Numb* RNA was unchanged between genotypes in the scRNA-seq libraries (Fig. 7a). However, the overall expression of NUMB protein decreased in *mdx* GFP$^+$ cells (Fig. 7c, d), and fewer

expressed NUMB (Fig. 7e). Although no differences in NUMB polarity were observed within the GFP$^+$ NUMB$^+$ fMuSC population (Fig. 7f), fewer *mdx* GFP$^+$ cells with polarized NUMB were present in the total GFP$^+$ fMuSC population (Fig. 7g). These findings suggest that dystrophin deficiency leads to NUMB downregulation, ultimately reducing the number of fMuSCs with polarized NUMB distribution.
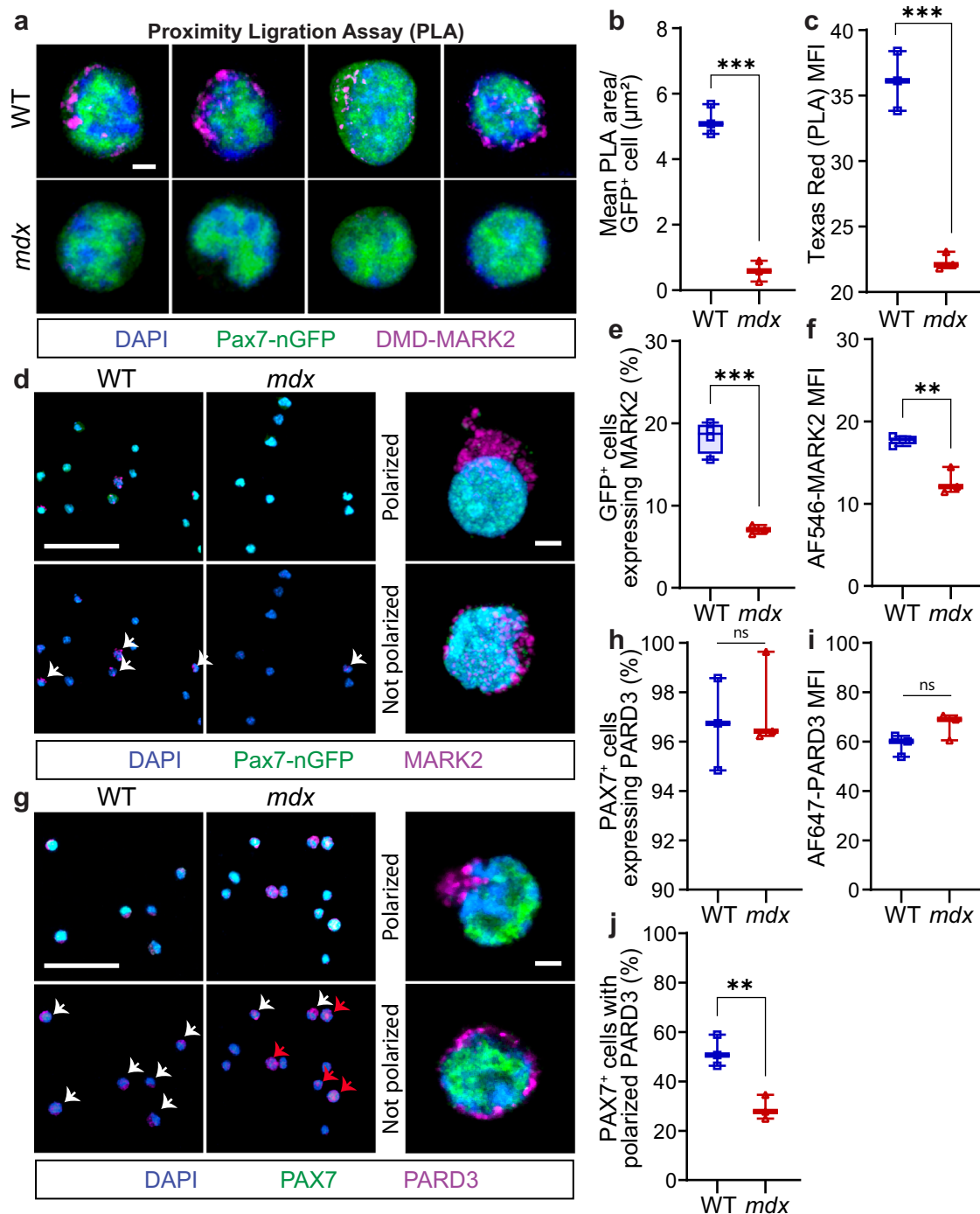
Fig. 6 | Absence of dystrophin disrupts fetal MuSC polarity. a Proximity ligation assay (PLA; magenta) performed on wild type (WT) and *mdx* GFP⁺ (green) cells isolated from E17.5 *Pax7-nGFP* fetal limbs using antibodies specific to MARK2 and repeats 8 and 9 of DMD (DMD^ex27/28). Cells counterstained with DAPI. Scale bar, 2 μm. **b** Mean PLA fluorescence area per cell measured in μm². **c** Mean fluorescence intensity (MFI) of PLA reaction in Texas Red in GFP⁺ cells. For **b**, **c**, *n* = 3 biological replicates with 185 WT and 125 *mdx* individual cells examined. **d** Representative immunofluorescence images of GFP⁺ (green) cells isolated from E17.5 *Pax7-nGFP* fetal limbs expressing MARK2 protein (magenta). Scale bars, 50 μm (left) and 2 μm (right). **e** Proportion of E17.5 GFP⁺ cells expressing MARK2 protein. **f** MFI of MARK2-

Alexa Fluor (AF) 546 in GFP⁺ cells. For **d**–**f**, WT *n* = 4 and *mdx n* = 3. For **e** and **f**, greater than 300 cells per replicate were enumerated. **g** Immunofluorescence staining of PAX7⁺ cells (green) expressing PARD3 (magenta). Scale bars, 50 μm (left) and 2 μm (right). **h** Proportion of PAX7⁺ cells that express PARD3. **i** MFI of PARD3-AF546 in GFP⁺ cells. **j** Proportion of PAX7⁺ cells expressing polarized PARD3. For **h**–**j**, greater than 150 cells assessed per replicate, and *n* = 3 per genotype. Statistical analysis performed using two-tailed unpaired *t*tests (** *p* < 0.01, ***p* < 0.001, ns = not significant). Box plots show the median, the 25th and 75th percentiles, and whiskers are the minimum and maximum values. Exact *p*values included in the **Source Data**.

Aak1 ablation rescues progenitor generation

During embryonic and adult myogenesis, NUMB polarization in MuSCs is believed to asymmetrically inhibit Notch signaling, thereby promoting asymmetric cell division and the generation of myogenic progenitors[43–46]. Considering that NUMB is a known Notch inhibitor

that plays a role in asymmetric cell divisions[40,41], and that both *Hes1* and *Notch3* are upregulated genes in *mdx* scRNA-seq libraries (Fig. 7a, b, Supplementary Data 3), we hypothesized that modulating NUMB expression and polarization could rescue the generation of myogenic progenitors in *mdx* fetal muscle.
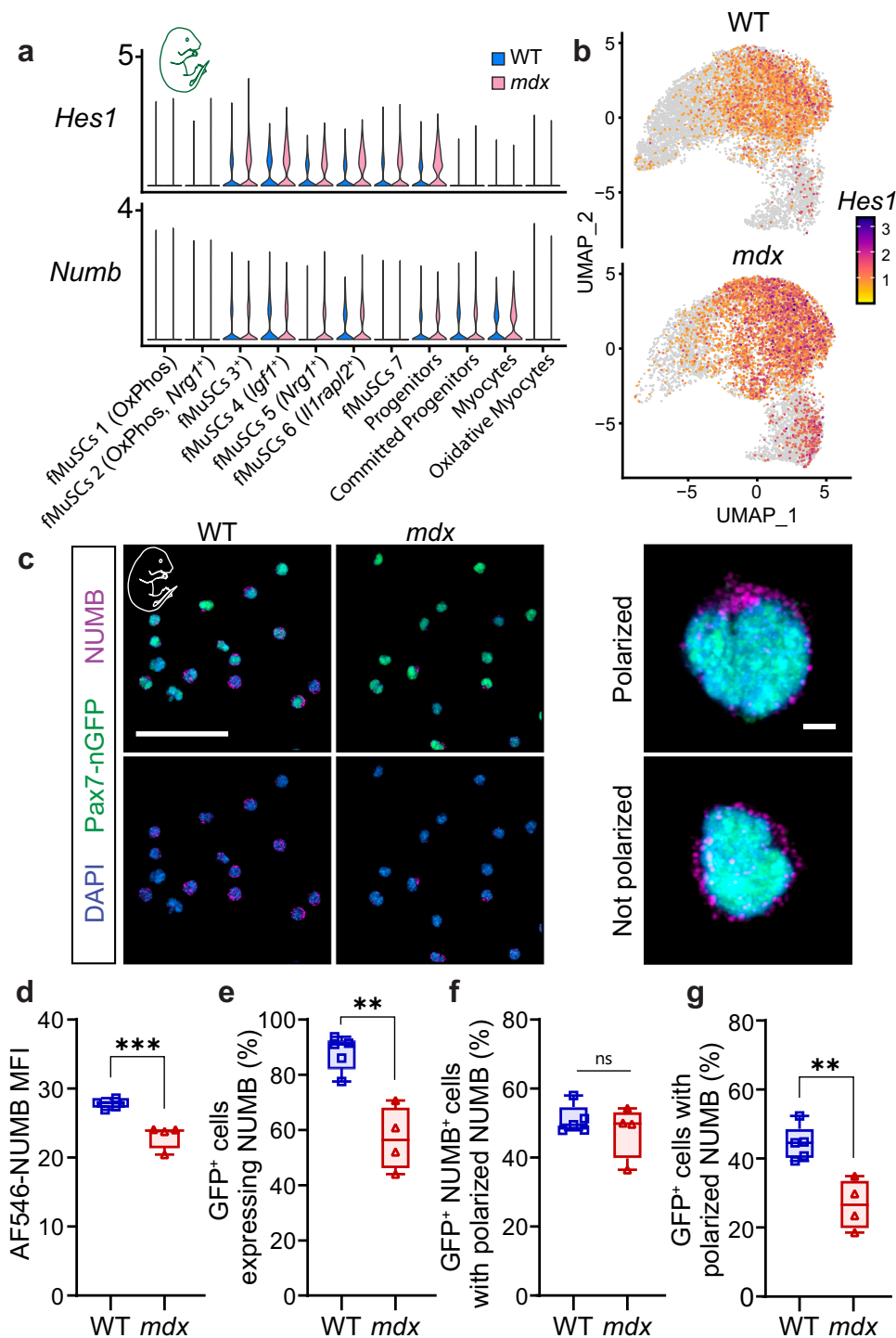
Fig. 7 | Reduced NUMB expression and polarization in *mdx* fetal MuSCs. a Violin plot of *Hes1* and *Numb* expression in wild type (WT) and *mdx* scRNA-seq libraries derived from GFP⁺ cells isolated from *Pax7-nGFP* E17.5 limbs and split by cluster. **b** Feature plot of *Hes1* expression in WT and *mdx* scRNA-seq libraries derived from GFP⁺ cells isolated from *Pax7-nGFP* E17.5 limbs and split by genotype. In **a**, **b**, *n* = 2 biological replicates. **c** Left: Representative immunofluorescence images of GFP⁺ (green) cells isolated from E17.5 WT and *mdx:Pax7-nGFP* limbs expressing NUMB (magenta) and counterstained with DAPI. Scale bar, 50 μm. Right: Example 3D projected images of a fMuSC expressing polarized and non-polarized NUMB

expression. Scale bar, 2 μm. **d** Mean fluorescence intensity (MFI) of NUMB-Alexa Fluor (AF) 546 in GFP⁺ cells. **e** Proportion of GFP⁺ cells expressing NUMB. **f** Proportion of GFP⁺ NUMB⁺ cells expressing polarized NUMB. **g** Percent of entire GFP⁺ cells expressing polarized NUMB. Between 180 and 1600 cells assessed per replicate. *n* = 5 WT, *n* = 4 *mdx*. Statistical analysis performed using two-tailed unpaired *t*tests (** $p < 0.01$, *** $p < 0.001$, ns = not significant). Exact *p*values included in the **Source Data**. Box plots show the median, the 25th and 75th percentiles, and whiskers are the minimum and maximum values.

Drosophila numb associated kinase (NAK) regulates asymmetric cell division by modulating the association of Numb with cell membranes[47]. In mammals, the NAK family consists of four homologs; however, only AAK1 has been demonstrated to phosphorylate NUMB[48].

Importantly, AAK1 is the closest ortholog to *drosophila* NAK and a positive regulator of Notch signaling that phosphorylates and antagonizes NUMB. Mutation of the AAK1 phosphorylation site and down-regulation of the *Aak1* gene result in a marked increase in membrane
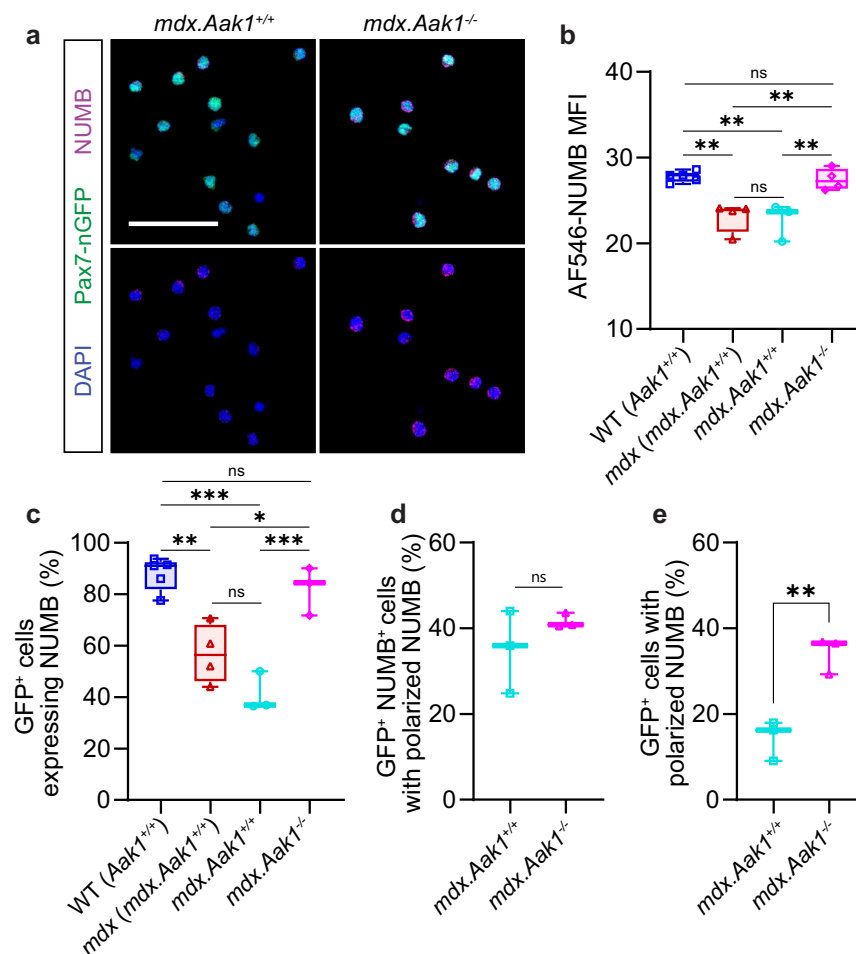
Fig. 8 | Fetal MuSC polarity rescued by the loss of AAK1 in *mdx* muscle.
a Immunofluorescence images of GFP⁺ (green) cells isolated from E17.5 *mdx:Pax7-nGFP.Aak1⁺/⁺* and *mdx:Pax7-nGFP.Aak1⁻/⁻* fetal limbs. Cells express NUMB (magenta) and are counterstained with DAPI. Scale bar, 50 μm. For **b**, **c**, WT (*Aak1⁺/⁺*) and *mdx* (*mdx:Aak1⁺/⁺*) conditions repeated from Fig. 2e, and *mdx:Aak1⁺/⁺* and *mdx:Aak1⁻/⁻* hindlimb muscles were analyzed separately. **b** Mean fluorescence intensity (MFI) of NUMB-Alexa Fluor (AF) 546 in GFP⁺ cells. **c** Proportion of GFP⁺ cells isolated expressing NUMB. **d** Proportion of GFP⁺ NUMB⁺ cells expressing polarized NUMB. **e** Percent of GFP⁺ cell population expressing polarized NUMB. Between 362 and 929 cells were assessed per replicate. Box plots show the median, the 25th and 75th percentiles, and whiskers are the minimum and maximum values. In **b**, **c**, $n = 5$ WT (*Aak1⁺/⁺*) and $n = 4$ *mdx* (*mdx:Aak1⁺/⁺*). In **a**, **b**, $n = 3$ *mdx:Aak1⁺/⁺* and $n = 4$ *mdx:Aak1⁻/⁻*. In **c–e**, $n = 3$ *mdx:Aak1⁺/⁺* and *mdx:Aak1⁻/⁻*. Data in **b**, **c**, were analyzed using a two-way ANOVA corrected for multiple comparisons using Sidak's post hoc test, and **d**, **e** were analyzed by two-tailed unpaired *t* tests. For all statistical tests, * $p < 0.05$ ** $p < 0.01$, *** $p < 0.001$ and ns = not significant. Exact *p* values included in the **Source Data**.

localization of NUMB[48–50]. Moreover, the polarized accumulation of NUMB during cell division promotes asymmetric daughter cell fates[41]. Therefore, we asked whether targeting AAK1 could restore the polarization of *mdx* fMuSCs.

We hypothesized that the loss of *Aak1* expression leads to increased asymmetric NUMB accumulation, thereby rescuing cell polarity and myogenic cell commitment. To investigate whether the loss of *Aak1* expression leads to increased NUMB polarization, we crossed the *mdx:Aak1⁻/⁻* and *Pax7-nGFP* lines to facilitate the isolation of fMuSCs. We then isolated GFP⁺ cells from *mdx:Pax7-nGFP:Aak1⁺/⁺* and *mdx:Pax7-nGFP:Aak1⁻/⁻* fetal limbs and assessed the expression of NUMB (Fig. 8a). Interestingly, the loss of *Aak1* expression restored both NUMB expression (Fig. 8b) and the proportion of GFP⁺ cells expressing NUMB to WT levels (Fig. 8c). In GFP⁺ cells expressing NUMB, polarization was comparable between all the genotypes assessed (Figs. 7g, 8c). However, we observed a significant 2.4-fold increase in the proportion of GFP⁺ myogenic cells exhibiting polarized NUMB, consistent with the overall increase in GFP⁺ cells expressing NUMB (Fig. 8e).

Quantification of PAX7⁺ and MYOG⁺ cells on E17.5 EDL and TA cross-sections revealed that while the loss of AAK1 had no impact on the number of PAX7⁺ cells, it resulted in a 30% increase in MYOG⁺ cells (Fig. 9c, d). The similar number of PAX7⁺ cells between genotypes suggests that the loss of AAK1 does not cause precocious differentiation or depletion of the fMuSC pool. We then compared the proportion of MYOG⁺ cells within the total PAX7⁺ and MYOG⁺ population between *mdx:Aak1⁺/⁺* and *mdx:Aak1⁻/⁻* fetuses. Not only was the proportion of committed MYOG⁺ cells elevated in *mdx:Aak1⁻/⁻* fetal muscle, but the loss of AAK1 restored the proportion to WT levels (Fig. 9e).

Analysis of the myofiber caliber distribution in hindlimb muscles of E17.5 *mdx:Aak1⁺/⁺* and *mdx:Aak1⁻/⁻* fetuses revealed a reduction in small-caliber myofibers, leading to a decreased proportion of smaller myofibers and an increased proportion of larger myofibers (Fig. 9f,g). The myofibers were also denser in *mdx:Aak1⁻/⁻* fetal muscle compared to *mdx:Aak1⁺/⁺* (Fig. 9f, Supplementary Fig. 10a). Corroborating our histological findings, RT-qPCR analysis on GFP⁺ cells isolated from E17.5 *mdx:Pax7-nGFP.Aak1⁺/⁺* and *mdx:Pax7-nGFP.Aak1⁻/⁻* fetal limbs also revealed no difference in *Pax7* expression between genotypes,
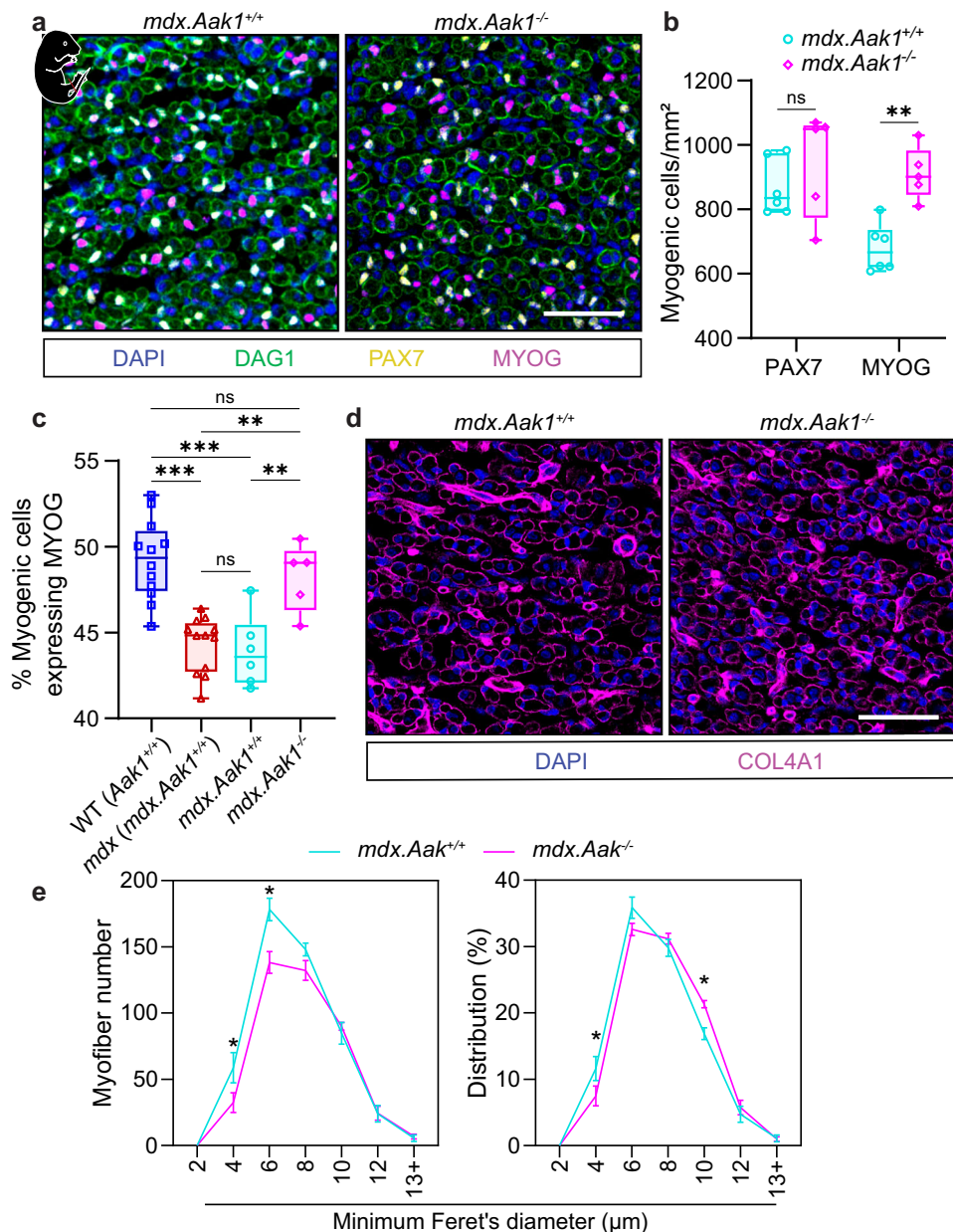
Fig. 9 | Removal of AAK1 restores myogenic progenitors in *mdx* fetal muscle.
a Immunostaining illustration of the E17.5 *extensor digitorum longus* (EDL) on hindlimb cross-sections derived from *mdx:Aak1⁺ᐟ⁺* and *mdx:Aak1⁻ᐟ⁻* fetuses. PAX7 (yellow) marks fetal MuSCs and MYOG (magenta) denotes differentiating myogenic cells. **b** Enumeration of myogenic cells expressing PAX7 and MYOG on *tibialis anterior* (TA) and EDL cross-sections, normalized to cross-section area (mm²). **c** Proportion of MYOG⁺ cells relative to entire PAX7⁺ and MYOG⁺ cell population at E17.5. WT (*Aak1⁺ᐟ⁺*) and *mdx* (*mdx:Aak1⁺ᐟ⁺*) conditions repeated from Fig. 2e (*n* = 12 per genotype), and *mdx:Aak1⁺ᐟ⁺* and *mdx:Aak1⁻ᐟ⁻* hindlimb muscles were analyzed separately. In **a**–**c**, *n* = 6 *mdx:Aak1⁺ᐟ⁺* and *n* = 5 *mdx:Aak1⁻ᐟ⁻*. **d** Representative immunostaining illustration of the E17.5 EDL on hindlimb cross-sections derived from *mdx:Aak1⁺ᐟ⁺* and *mdx:Aak1⁻ᐟ⁻* fetuses. Extracellular matrix marked by COL4A1 staining (magenta), and counterstained with DAPI (blue). **e** Distribution of myofiber size using minimum Feret's diameter by number of myofibers (left) and proportional distribution (right). For **d**, **e**, *n* = 4 *mdx:Aak1⁺ᐟ⁺* and *n* = 5 *mdx:Aak1⁻ᐟ⁻*. For **b**, **c**, box plots show the median, the 25th and 75th percentiles, and whiskers are the minimum and maximum values. For **e**, data presented as mean values ± SEM. Data analyzed in (**b** and **e**) using a two-way ANOVA corrected for multiple comparisons using Sidak's post hoc test. For **c**, data was analyzed using one-way ANOVA corrected for multiple comparisons using Tukey's test. Significance: $*p < 0.05$, $**p < 0.01$, $***p < 0.001$, ns = not significant. Exact *p*values included in the **Source Data**. Scale bars, 50 μm.

while *Myog* expression was significantly increased in the *mdx:Aak1⁻ᐟ⁻* cells (Supplementary Fig. 10b).

Our data suggest that modulating AAK1 activity in the *mdx* fetus restores NUMB expression and polarity, together with increased numbers of differentiation-competent progenitors during secondary myogenesis. These findings support the conclusion that disrupted muscle development during secondary myogenesis is largely due to intrinsic fMuSC dysfunction resulting from the absence of dystrophin.

Discussion

Our comprehensive study of myogenesis in the *mdx* embryo reveals that DMD is an intrinsic MuSC disease that manifests during secondary myogenesis before any accumulation of necrotic myofibers, fibrosis, or inflammatory changes[19]. Our findings suggest that dystrophin does not play any role in primary myogenesis. Indeed, full-length dystrophin is undetectable by western blot at E10.5. Furthermore, full-length dystrophin is first upregulated in *Pax7⁺* cells at E14.5, coinciding with

the onset of secondary myogenesis. This timing aligns with the initial detection of a basal lamina surrounding muscle fibers at E14.5[26], and reports that fetal myogenic progenitors are enriched in adhesion-related genes[51]. Together, this reaffirms that distinct mechanisms govern the growth and repair of embryonic, fetal, and adult muscle.

Unlike embryonic myofibers, a basal lamina surrounds the dermomyotome, and dermomyotome cells undergo symmetric and asymmetric cell divisions[46,52,53]. While full-length dystrophin is not expressed and does not regulate dermomyotome cell specification, dystroglycan and full-length utrophin are present at the dermomyotome basal lamina. Because both proteins are known interactors with MARK2 and play a role in polarizing other epithelial structures, dystroglycan and utrophin may regulate dermomyotome polarity[4,38,54]. However, while dystrophin has a high affinity for binding microtubules, utrophin does not, suggesting utrophin likely does not play a role in mitotic spindle orientation[55].

Recent modeling of somitogenesis using hiPSCs discovered the expression of a truncated 412kDA embryonic dystrophin isoform (Dp412e) in cultured mesoderm cells and embryoid bodies shortly before expression of full-length muscle dystrophin[56]. Similar experiments using DMD patient-derived hiPSCs observed the downregulation of somite markers, suggesting that dystrophin plays a role upstream of primary myogenesis[17]. While the promoter of Dp412e, located on exon 6 of the human *DMD* gene, is unique to select arthropods, including humans[56], full-length muscle dystrophin is also expressed during both mouse and human development[9,10]. Interestingly, murine presomitic and somitic mesoderm cells extracted from a recently published E8.5 single cell sci-RNAseq3 dataset express the *Dmd* transcript[57]. However, the murine *Dmd* gene does not contain the exon 6 embryonic promoter, and the sci-RNA-seq3 techniques enrich 3' RNA reads, necessitating further investigation. Nevertheless, an upstream role for dystrophin, perhaps in the presegmental plate, could explain the difference we observed in somite number and limb ontology. Alternatively, the absence of dystrophin in *mdx* dams could impact embryonic development. However, we did not further explore the biological relevance of this staging difference.

Compared to the WT fetus, the pathology of *mdx* muscle differs at the beginning and end of secondary myogenesis. In addition to reduced laminin staining, we see a more pronounced reduction in total myogenic cells in *mdx* muscle at E14.5 compared to E17.5. Several lines of evidence indicate that the transition from primary to secondary myogenesis is not delayed in the *mdx* fetus. WT and *mdx* myogenic cells express similar levels of *Nfix* at E14.5. Moreover, the same number of MYH7^{+} myofibers was observed in WT and *mdx* fetal muscle. We therefore conclude that the phenotypic differences between E14.5 and E17.5 result from a cumulative effect of polarity impairment that begins at E14.5 and persists throughout secondary myogenesis. This is evidenced by the reduced PARD3 polarization in E14.5 *mdx* fMuSCs and the decreased numbers of progenitor cells enumerated on E14.5 *mdx* cross-sections.

In adult muscle, an increased number of FAPs is thought to result from chronic exposure to the dystrophin-deficient environment, contributing to progressive fibrosis with age[58]. Interestingly, in *mdx* and DMD fetal muscle, decreased myofiber density is accompanied by increased ECM deposition despite the absence of necrosis or muscular damage[12,15]. Similarly, *mdx* fetal muscle is visibly less dense than WT muscle. Interestingly, our scRNA-seq analysis reveals a fFAP population representing 1.3% of the WT and 2.1% of the *mdx* libraries, respectively. Given that fFAPs can originate from *Pax7*^{+} lineages[59], the significance of this population in *mdx* muscle remains an interesting question.

Building on our previous discoveries[4,6,8], we find that the polarity and progenitor deficits observed in adult myogenesis begin during fetal development and profoundly affect secondary myogenesis[4]. The loss of dystrophin-MARK2 interactions in fMuSCs leads to the downregulation of MARK2, disrupted PARD3 polarization, and the

generation of fewer proliferating and committed progenitor cells. Moreover, we see an expansion of uncommitted *Myf5*-low fMuSCs in *mdx* fetal muscle by histological and single cell transcriptomic analysis. Thus, the overall reduction in PAX7^{+} cells that occurs during secondary myogenesis is a direct result of fewer proliferating progenitors, and not depletion of the fMuSC pool. The reduction in myogenic progenitor generation also provides a plausible explanation for the hypotrophic myofibers observed in *mdx* mice during fetal and neonatal development[25].

A recently published preprint describing a conditional *Dmd* allele presents an opportunity for future studies to study the cell-intrinsic functions of DMD during MuSC polarity establishment, asymmetric cell divisions, and fate specification[60]. While the current study utilizes the constitutive *mdx* model to assess the consequences of dystrophin loss, this mouse model will enable an analysis of DMD's intrinsic role in MuSCs.

Several differences in developmental timelines between mice and humans are notable and relevant to interpreting dystrophin's role during myogenesis. The transition from primary to secondary myogenesis occurs around E14.5 in mice, and fetal myogenesis spans approximately 30% of gestation. In contrast, the transition occurs between 7 and 12 weeks in humans, encompassing 70–80% of *in utero* development[61]. Analysis of previously published Drop-seq data reveals that the *DMD* transcript is enriched in human PAX7-expressing cells at fetal, but not embryonic, time points, consistent with the notion that dystrophin plays a role in fetal rather than embryonic PAX7^{+} populations[61]. The prolonged duration of human fetal myogenesis may amplify any impact of dystrophin deficiency on secondary myogenesis.

Studies of mammalian neurogenesis find that PARD3 is an upstream regulator of Notch signaling that requires the expression of *Numb* and *Numbl* to promote asymmetric cell fate[39]. Ectopic expression of *Pard3* increases Notch signaling, while loss of *Pard3* expression leads to its downregulation. However, the loss of *Numb* and *Numbl* abolishes the effect of *Pard3* knockdown, leading to elevated Notch signaling in the absence of PARD3. Moreover, studies in mammalian cells demonstrate that NUMB is phosphorylated by the PAR-complex protein aPKC, which is dependent on PARD3, and leads to the asymmetric distribution of NUMB and aPKC/PARD3[62,63]. Thus, disrupted PARD3 polarity could conceivably lead to the downregulation of NUMB in the entire *mdx* fMuSC population. The mechanistic relationship between the loss of MARK2-dystrophin interactions and NUMB remains unclear, making it an interesting topic for future investigation. Notably, NUMB has been shown to sequester MARK2 at the cell membrane in human hepatocyte cells[64].

While the loss of Notch signaling in MuSCs promotes precocious differentiation[65], Notch pathway gene mutations can ameliorate dystrophic phenotypes. For instance, the Golden Retriever muscular dystrophy model of DMD typically displays a very severe pathology that leads to cardiorespiratory failure and death before 2 years of age. However, 'escaper' dogs carrying a disease-modifying mutation to the *Jag1* gene lived long and healthy lifespans[66]. We find that targeting the NUMB inhibitor gene *Aak1* can rescue myogenic progenitor formation in the *mdx* fetus. Loss of *Aak1* increases NUMB expression and polarity in *mdx* fMuSCs, in addition to restoring the balance of PAX7^{+} fMuSCs to committed MYOG[+] progenitors without depleting the stem cell pool. While the precise mechanisms remain to be fully elucidated, given the role of AAK1 in negatively regulating NUMB membrane localization[49] and the observed increase in NUMB MFI in the AAK1-null fMuSCs, we hypothesize that NUMB directly restores fMuSC polarity independently of DMD-MARK2.

Based on our findings, we hypothesize that the loss of *Aak1* expression counteracts the inhibitory effect of the PAR complex on NUMB, allowing fMuSCs to respond to asymmetric Notch ligand cues in the niche and undergo asymmetric division. This hypothesis is based

on the finding that Notch ligands from the basal niche and apical myofiber module MuSC behavior, and that self-renewing *Myf5*-low MuSCs express higher levels of NOTCH3 than *Myf5*-high primed MuSCs[23]. Conceivably, DLL4 from endothelial cells modulates the self-renewal of *Myf5*-low fMuSCs basally during asymmetric cell division, while either reduced DLL4 presented by the myofiber or expression of other Notch ligands stimulates proliferation and commitment of the *Myf5*-high fMuSCs. Thus, AAK1 represents an attractive therapeutic target.

Our findings provide compelling evidence that DMD is an intrinsic MuSC disorder characterized by deficits in MuSC polarity and myogenic progenitor generation that begin during secondary myogenesis. Since MuSC dysfunction and aberrant muscle architecture arise *in utero*, it may be essential to implement newborn screening for DMD followed by MuSC-targeted therapies administered shortly after birth to leverage rapid neonatal muscle growth and enable timely intervention.

Methods

Materials and correspondence
Resources and reagent requests should be directed to and will be fulfilled by the corresponding contact, Michael Rudnicki (mrudnicki@ohri.ca). Please see Supplementary Table 1 for the list of antibodies, Supplementary Table 2 for other product details, Supplementary Table 3 for primers, and Supplementary Table 4 for mouse strains. All relevant software is listed in Supplementary Table 5.

Experimental approval, models, and procedures
All housing, husbandry, and experiments were performed in accordance with the University of Ottawa Animal Care Committee guidelines and approved by Animal Research Ethics Board at the University of Ottawa. The following mouse lines were used: C57BL/10ScSnJ (referred as WT, JAX #000476), C57BL/10ScSn-Dmd^mdx/J (referred as *mdx*; JAX #001801), *Pax7-nGFP* (JAX #036759)[67], *ROSA-nTnG* (JAX #023035)[68], *Myf5-Cre* (JAX #007893)[69], and *Aak1^tm1a(EUCOMM)Hmgu* (*Aak1*^−/−, EMMA ID #EM:08493)[70]. All transgenic lines were bred onto the *mdx* background before timed mating experiments.

Male and female adult *Pax7-nGFP* mice were used in equal numbers between 10 and 20 weeks-of-age. To induce muscle injury, adult mice were anesthetized using isoflurane in 1% oxygen, then injected with 50 μL of 10 μM Cardiotoxin (CTX) solution (Latoxan) directly into the TA and 100 μL into the *gastrocnemius* muscle. For analgesia, mice were administered 50 μL of 5 mg/mL carprofen before the procedure. Mice were euthanized 48 h following injury.

Timed mating was performed using post-coital plug visualization, with the day of conception assigned as E0.5. To reduce false-positive pregnancies at early time points, maternal weight was measured at days E0.5 and E9.5. A threshold weight gain of 1.75 g at E9.5 was used to determine pregnancy[71]. On the day of embryo collection, pregnant mice were humanely euthanized and c-sectioned, and the embryos were removed at corresponding time points between E10.5 and E17.5. All embryos were immediately placed in ice-cold PBS, and fetal mice were euthanized by decapitation. To obtain neonatal mice, breeding pairs were monitored for births after 18 days in the same enclosure. The day of discovery was labeled as perinatal day 0 (P0). Perinatal mice (P7) were euthanized by decapitation. All experiments using embryonic, fetal, and neonatal mice were conducted post-mortem. Both male and female embryos and neonates were used in equal numbers for comparative analysis. Due to the nature of embryo isolation, samples were collected before the genetic sex of the embryos was determined.

Genotyping
Genetic sex. The DNA extraction and PCR protocol for determining genetic sex was adapted from previously published methods[72]. SX primers amplified intron 8 of *Sly* on the Y chromosome (~ 300 bps)

and intron 6 of *Xlr* 6 on the X chromosome (~ 500–700 bps). The PCR primer pairs were as follows: SX_F, 5′-G ATGATTTGAGTGGAAATGT-GAGGTA-3′;SX_ R, 5′CTTATGTTTATAGGCATGCACCATGTA-3′. DNA was extracted from portions of the yolk sac or tail. The tissue was placed in 200 μL of DNA extraction buffer (50 mM KCl, 10 mM Tris-HCl pH8.3, 2.5 mM MgCl₂, 0.1 mg/mL gelatin, 0.45% (v/v) Nonidet P-40, 0.45% (v/v) Tween-20; autoclaved and stored frozen) supplemented with 150 μg/mL proteinase K. Samples were incubated at 55 °C, vertexing every 15 min for 1 h then overnight. The proteinase K was then heat-inactivated at 95 °C for 5 min. DNA was diluted 5X, then 1 μL of each sample was added directly to a PCR reaction. The PCR reaction was performed in a final volume of 25 μL with High-Fidelity Phusion Polymerase (Thermo Fisher Scientific), 1X Phusion buffer, 1 μL DMSO, 0.2 mM dNTPs, 0.5 μM primers and 1 μL DNA. The PCR parameters were as follows: initial denaturation at 94 °C for 2 min, 35 cycles with 94 °C for 30 s, 57 °C for 30 s, and 72 °C for 30 s, followed by final elongation at 72 °C for 5 min. The PCR product was electrophoresed with 1 Kb Plus DNA Ladder (Invitrogen) on a 2% agarose gel with ethidium bromide and visualised using UV-illumination.

Aak1 mutants. Genotyping for *Aak1* mutants requires the purification of DNA from tissues. According to the manufacturer's protocol, DNA was extracted from fetal tail clippings using the NucleoSpin Tissue kit for DNA from cells and tissue (Macherey-Nagal). *Aak1* primers are listed in Supplementary Table 3. The PCR products were 328 bps for the WT and 392 bps for the mutant allele. The PCR reaction was performed in a final volume of 20 μL with High-Fidelity Phusion Polymerase (Thermo Fisher Scientific), 1X Phusion buffer, 1 μL DMSO, 0.2 mM dNTPs, 2 μM primers and 2 μL DNA. The PCR parameters were as follows: initial denaturation at 94 °C for 4 min, 35 cycles with 94 °C for 30 s, 62 °C for 30 s, and 72 °C for 1 min, followed by final elongation at 72 °C for 7 min. The PCR product was electrophoresed with 1 Kb Plus DNA Ladder (Invitrogen) on a 2% agarose gel with ethidium bromide and visualized using UV illumination.

Embryo staging
Fixed embryos were visualized for embryo staging using a Zeiss Stereo Discovery V8 microscope equipped with an achromat S 1,0X objective. Images were acquired using AxioVision software. Somites were enumerated manually using FIJI, and limb ontology staging was conducted using the forelimb and the Embryonic Mouse Ontogenetic Staging System (https://limbstaging.embl.es/).[21]

Fluorescence-activated cell sorting (FACS)
MuSCs isolated from uninjured and CTX-injured adult *Pax7-nGFP* hindlimb muscles were dissected, minced briefly, and dissociated in Hams F10 (Wisent) containing collagenase/dispase using a gentle MACS Octo Dissociator (Miltenyi Biotec). A single cell suspension was generated by filtering and centrifugation. The cell pellet was also treated with red blood cell lysis buffer according to the manufacturer's recommendation (Sigma, Hybri-Max). Staining with lineage-negative (Lin⁻) antibodies against CD31, CD11b, CD45, and SCA1 conjugated to BV421 (BD Biosciences) was performed in 1 mL of FACS buffer (5% FBS, 5 mM EDTA in PBS), followed by 7-Aminoactinomycin D (7-AAD) (STEM CELL Technologies, 75001.1) viability dye staining. Viable GFP⁺ Lin⁻ cells were then isolated using a MoFlo XDP cell sorter (Beckman Coulter).

Embryonic tissue was manually dissociated in 3 mL of collagenase/dispase solution using razor blades. Fetal limbs were dissociated in 3 mL of collagenase/dispase-containing medium using a gentle MACS Octo Dissociator (Miltenyi Biotec 130-095-937). From this point, three conditions were used to isolate embryonic and fetal MuSCs. For all assays not examining protein polarity, GFP⁺ cells stained with 7-AAD were isolated from the trunk and limbs (embryonic time-points) or the limbs (fetal timepoints) of *Pax7-nGFP* mice. A second method was employed for experiments examining protein polarity.

GFP+ cells were isolated from *Pax7-nGFP* hindlimb muscle that were dissociated, filtered, stained with the fixable viability Zombie NI dye (BioLegend), and formaldehyde-fixed (4% PFA) before cell sorting. Finally, the MARK2 and dystrophin polarity analysis shown in Fig. 5e was conducted on E17.5 PAX7+ cells isolated from WT and *mdx* fetal limbs. Following limb dissociation, filtering, and fixation, the cell pellet was stained overnight with antibodies against lineage negative (Lin⁻) markers (CD31, CD11b, CD45, SCA1) conjugated to PE-Cy7 (BD Biosciences) and unconjugated PAX7 (HDSB), followed by 1 h of staining with a AlexaFluor secondary antibody. All cells were isolated with a MoFlo XDP cell sorter (Beckman Coulter). Notably, we find that fMuSCs retain apical-basal polarity following a short 25 min tissue dissociation. However, tissue dissociation before formaldehyde fixation may alter the cell morphology. Antibodies are listed in Supplementary Table 1.

Single cell assays
Fixed and live isolated WT and *mdx* myogenic cells were adhered to 12-well removable chambers Ibidi slides coated with Corning Cell-Tak for immunostaining, RNA scope, and proximity ligation assay (PLA). Following adhesion, live cells were fixed with 4% paraformaldehyde for 20 min at RT.

NIH 3T3 cells, used as negative control cells for the single cell assays, were grown on 12-well chambers slides in high-glucose DMEM supplemented with 10% FBS and 1% penicillin/streptomycin. The cells were then fixed with 4% paraformaldehyde for 20 min at RT.

Immunostaining. Immunostaining was modified from previously described methods[73]. Fixed cells were permeabilized (0.1% Triton X-100, 0.1 M Glycine in PBS), blocked (5% horse serum, 2% BSA, and 0.1% Triton X-100 in PBS), and stained overnight at 4 °C in blocking buffer with a combination of primary antibodies against EGFP, MARK2, NUMB, DMD, and PAX7. The following day, the cells were incubated with Alexa Fluor-conjugated secondary antibodies (1:1500) for 1 h at room temperature (RT), counterstained with DAPI (0.5 µg/mL in PBS) and mounted with PermaFluor (Fisher). Antibodies are listed in Supplementary Table 1.

RNAscope. In situ hybridization assays using the RNAscope Multiplex Fluorescent Reagent Kit v2 (Advanced Cell Diagnostics) kit were conducted according to the manufacturer's protocol for cultured adherent cell samples. Protease III was diluted 1:15 and incubated for 10 min. Probes that target *Pax7* (RNAscope Probe- Mm-Pax7-C2, ACD) and exons 4–10 of the full-length *Dmd* (*Dmd*ᵉˣ⁴⁻¹⁰) (RNAscope Probe- Mm-Dmd, ACD) were used. Control 3T3 cells that do not express *Pax7* or appreciable *Dmd* were assayed in parallel[74]. The cells were counterstained with DAPI (0.5 µg/mL in PBS) and mounted with PermaFluor (Fisher).

Proximity ligation assay (PLA). Cells were permeabilized, blocked using Duolink Blocking solution for one hour at 37 °C, then incubated in Duolink Antibody diluent containing primary antibodies against GFP (Abcam; 1:1500, Cat# ab13970), MARK2 (LS Bio, 1:1000, #LS-B7503; 1:1000), and DMD (MANDYS16; 1:10, DSHB; # AB_2618166) overnight at 4 °C. PLA was then performed using Duolink mouse plus and rabbit minus probes, and the assay was conducted using the In Situ Detection Reagents in Texas Red (Duolink; # DUO92008) according to the manufacturer's guidelines. Secondary antibodies against GFP were added to the PLA amplification step. The cells were counterstained with DAPI (0.5 µg/mL in PBS) and mounted with PermaFluor (Fisher).

Image acquisition and analysis. All single cell assays were imaged on a Zeiss LSM900 confocal microscope with Z-stacks using a Plan-Apochromat 20X/0.8 M27 objective in conventional pinhole microscopy mode. Where possible, all image analysis was automated using

IMARIS and FIJI software. To analyze cell polarity, where cells were assigned a polarity status manually, all images were blinded by a third party with no knowledge of the experimental details. A threshold mask was assigned to each replicate in FIJI, which was used to determine cell polarity. Cells were considered polarized if staining was restricted to half or less of the cell.

High magnification images were acquired using a Plan-Apochromat 63X/1.4 NA Oil objective and Zeiss Airyscan 2 Super Resolution technology. Airyscan processing was performed using Zen 3.7 Blue Edition software and the Image Analysis module.

RNA extraction and RT-qPCR
Total RNA was extracted from approximately 100,000 (E14.5) and 250,000 (E17.5) sorted GFP+ cells isolated from *Pax7-nGFP* fetal limbs using the PicoPure RNA Isolation Kit (Life Technologies Inc). For these experiments, WT, *mdx*, *mdx:Aak1*⁺/⁺ and *mdx:Aak1*⁻/⁻ lines were crossed with *Pax7-nGFP* transgenic mice. Reverse transcriptase cDNA was synthesized using the iSCRIPT Synthesis Kit (Bio-Rad). The RT-qPCR reaction was performed in a final volume of 20 µL with SYBR Green PCR Master Mix (Bio-Rad), ROX reference dye (Invitrogen), 0.5 µM primers and DNA diluted 1:10. The PCR parameters were as follows: 95 °C for 3 min, 40 cycles with 95 °C for 20 s, 58 °C for 20 s, and 72 °C for 30 s, then 95 °C for 10 s, and melt curve at 65 °C for 5 s and 95 °C for 5 s. *Tbp* and *Gapdh* were used as reference genes at E14.5, while *Rps18* and *Ppia* were used as reference genes at E17.5. Primers used for RT-qPCR were published and are listed in Supplementary Table 3[75,76]. RT-qPCR experiments were performed using the Bio-Rad CFX96 or CFX384 Detection System in combination with the CFX Maestro 1.1 software for data acquisition. Analysis was performed using the $2^{-\Delta\Delta Ct}$ method.

Cross-section immunostaining
All cross-section staining protocols were previously described[73]. Tissues from embryos and fetal limbs were processed differently. Embryos were embedded in paraffin, while fetal limbs were cryopreserved.

Embryo tissue processing and staining. E10.5 embryos were fixed in fresh 4% PFA for 24 h, then sent to the Louise Pelletier Histology Core Facility at the University of Ottawa for paraffin embedding and sectioning. Four-micron sections were deparaffinized in xylene for 10 min and rehydrated in an ethanol series of 100% EtOH, 95% EtOH, 70% EtOH, and 50% EtOH for 5 min each at RT. Sections were rinsed in dH₂O, and antigen retrieval was performed using citrate buffer (10 mM Sodium Citrate, 0.05% Tween 20, pH 6.0) in a pressure cooker set to 12 psi for 10 mins. Sections were then permeabilized (0.1% Triton-X 100, 0.1 M Glycine in PBS) for 10 min, treated with 1X TrueBlack Lipofuscin Autofluorescence Quencher (Biotium; #23007) in 70% EtOH for 30–60 s, and incubated in blocking solution (5% horse serum, 2% BSA in PBS) for 1 h. M.O.M. blocking reagent (1:40; Vector Laboratories) was added to the blocking buffer for all stains using mouse primary antibodies. Primary antibodies were incubated overnight at 4 °C in blocking solution. The following primary antibodies were used: Laminin (1:500, Sigma), MF20 (DSHB, 1:10), Mandag2 (DSHB, 5 µg/mL), Utrn (BD biosciences, 1:200), PAX7 (DSHB,1:1), PAX3 (DSHB, 1:1), and MYOG (Abcam, 1:500). Isotype and species-specific cross-absorbed Alexa Fluor secondary antibodies were incubated for 1 h at RT, followed by DAPI (0.5 µg/mL in PBS) counterstaining and mounting in PermaFluor (Thermo Fisher Scientific). Cross-sections stained with PAX7 and MYOG antibodies were imaged using a Zeiss Axio Observer.D1 inverted microscope. Laminin and UTRN stained cross-sections were imaged on an LSM800.

Fetal limb processing and staining. Fetal and neonatal limbs were carefully cut from the body, immersed in 4% PFA for 12 h at 4 °C, and

placed in a sucrose gradient of 15% and 30% sucrose (w/V) in PBS overnight at 4 °C. The limbs were then embedded in OCT compound (Tissue-Tek), frozen in liquid nitrogen-cooled isopentane, stored at −80 °C, and sectioned at 10μm intervals. Antigen retrieval, described above, was performed when staining with an antibody that required epitope unmasking.

Sections were permeabilized for 10 min and incubated in blocking solution with M.O.M. blocking reagent (1:40) for 1 h. Primary antibodies were incubated overnight at 4 °C in blocking solution. The following primary antibodies were used: PAX7 (DSHB,1:1), MYOG (Abcam, 1:500), Laminin (Sigma, 1:500), DAG1 (Abcam; 5 μg/mL), and COL4A1 (Abcam; 1:500). Slides were incubated with cross absorbed Alexa fluor secondary antibodies in blocking buffer for 1 h at RT, followed by DAPI (0.5 μg/mL in PBS) counterstaining and mounting in PermaFluor (Thermo Fisher Scientific). Antibodies are listed in Supplementary Table 1.

Fetal cross-sections were imaged with a Zeiss Observer 7 widefield microscope or an LSM900 confocal microscope equipped with a Plan-Apochromat 20X/0.8 M27 objective. Automated cell counting was conducted using IMARIS software (v9) with the count spot function or the FIJI analyze particle function. Only one type of automation was used per individual experiment. Myofiber size analysis was conducted using IMARIS using the outline cell function and dystroglycan or COL4A1 staining.

Whole mount embryo immunostaining

Whole mount staining was modified from the 2016 iDISCO protocol (https://idisco.info/idisco-protocol/)[77]. Embryos were fixed in 4% PFA for 12 h, permeabilized (0.4% Tx-100, 10% DMSO and Glycine 0.1 M in PBS) for 4 h at RT, and blocked overnight at 4 °C (125 nM Glycine, 5% Donkey serum, 2% BSA, 0.2% Tx-100, and 5% DMSO in PBS). The embryos were then incubated in primary antibodies diluted in staining solution (5% DMSO, 3% Donkey Serum, and 0.2% Tween 20 in PBS) for 24 h at 4 °C. The following primary antibodies were used: PAX7 (HDSB), PAX3 (HDSB), MYOG (Abcam, 1:250), and dystroglycan (Mandag1, HDSB, 5 μg/mL). PAX3 and PAX7 hybridoma supernatants grown in the lab were purified using a commercial kit and used at a 10 μg/mL concentration (Abcam ab109207). Following extensive washes in PBS with 0.2% Tween (PSB-Tw) at RT, the embryos were incubated 24 h at 4 °C in AlexaFluor secondary antibodies diluted in staining solution. After additional washing, DAPI (1 μg/mL in staining solution) counterstaining was performed for 1 h at RT. Antibodies are listed in Supplementary Table 1.

Optical clearing was performed using a glycerol series of 20–90%, after which the embryos were mounted on glass slides in glycerol mounting media (90% glycerol, 0.5% N-propyl gallate in TBS pH 8.5). Images illustrated in Supplementary Fig. 1 were acquired using a Leica SP8 confocal microscope equipped with a galvo stage and a Plan-Apochromat 20X/0.75 IMM CORR CS2 objective. Automated cell counting was conducted using IMARIS software's count spot function (version 9). Supplementary Fig. 2c depicting dystroglycan whole mount staining was acquired using an LSM800 using a Plan-Apochromat 20X/0.8 M27 objective. For the immunofluorescence image illustrating single cells at 20X, FIJI's despeckle function or Gaussian filtering (sigma value of 1) was applied to 20X confocal images. The same processing was performed within each experiment.

Western blot

Adult mouse TA muscles and embryonic tissues were collected, snap frozen in liquid nitrogen, homogenized and extracted in RIPA lysis buffer (150 mM NaCl, 0.1% TritonX_100, 0.5% sodium deoxycholate, 0.1% SDS, 50 mM Tris_HCl pH8.0) supplemented with proteinase inhibitors (Roche) for 1 h on ice with vertexing every 10 min. Extracts were heated in Laemmli buffer for 5 min at 95 °C then resolved by SDS-PAGE, transferred to a PVDF membrane and analyzed by western blot

with antibodies against dystrophin (DYS1, Leica,1:20; c-terminal DMD, Abcam, 1:500), utrophin (BD Bioscience, 1:500) and GAPDH (1:1000). Blocking was done using 5% milk in TBST and primary antibodies were incubated overnight in. blocking buffer. Secondary antibodies conjugated to HRP (1:5000) were diluted in blocking buffer for 1 h. The blots were visualized using ECL with a BioRad digital imager. Antibody details are listed in Supplementary Table 1.

Single cell RNA-sequencing

The libraries were generated in biological duplicates using GFP^{+} cells isolated from WT and *mdx:Pax7-nGFP* fetal limbs with the 10X Genomics 3′ v3 platform. The libraries were sequenced to a mean read depth of 17,013 reads/cell using the Illumina NextSeq 500. Reads were aligned to the GENCODE vM25 (GRCm38/mm10) reference genome using CellRanger (v7.1.0) with default parameters.

Filtering, quality control and analysis were performed using R (v4.3.1) and the package Seurat (v5.1.0)[78,79]. The following were excluded from analysis: genes expressed in fewer than 3 cells, cells expressing fewer than 500 or greater than 5000 genes, and cells expressing greater than 20% mitochondrial genes. Doublets were also excluded using the package scDblFinder[80]. Following filtering, 10,921 and 11,168 cells were observed in the two WT libraries, respectively, while 10,292 and 15,050 cells remained in the two *mdx* libraries.

The combined libraries were normalized using SCTransform (v2)[81,82], after which we performed principal component analysis, Uniform Manifold Approximation Projection (UMAP) embedding with the top 30 principal components, and cell clustering with a resolution of 0.2. Custers were then annotated using known cell markers and Seurat's FindAllMarkers function, where cluster markers were input into online tools, including Metascape and gprofiler[83,84]. Mitosis S and G2/M phase scores were assigned using Seurat's CellCycleScoring function. A contaminating cluster of *Ptprc*^{+} immune cells and low-quality cells, characterized by lower relative nfeatures and ncount RNA and lack of meaningful biological identity, accounted for less than 2% of the libraries and were omitted from downstream analysis. Two additional clusters were excluded. The first were *Pax7*^{+} '*Tex14*^{+} Cells,' representing 3.3% and 2.3% of the WT and *mdx* libraries, respectively, and likely originated from the fetal testes[85,86]. The second were *Pdgfra*[+] *Cd34*^{+} fetal fibro-adipogenic progenitors ('fFAPs'), accounting for 1.3% of the WT and 2.1% of the *mdx* libraries. The five remaining clusters of myogenic identity.

Next, using Seurat's subset function, we analyzed the myogenic cell clusters alone. First, cell cycle regression was performed using SCTransform normalization, after which PCA analysis, UMAP embedding with the top 25 principal components, and clustering with a resolution of 0.6 was repeated. Clusters were annotated by known cell markers and Seurat's FindAllMarkers function. Graphics were generated using Seurat, SCpubr, and scCustomize[78,87,88]. Adobe Illustrator (v29) was used for minor edits to line size, text, and color.

Differential gene expression analysis between WT and *mdx* libraries was performed using Seurat's FindMarkers function, with default Wilcoxon test and a minimum expression threshold (min.pct) set to 0.1. An adjusted p value less than 0.05 was considered significant, and exact p values are provided in Supplementary Data 3. Functional analysis of enriched genes was conducted using Gene Ontology Biological Processes[89,90], and the R application clusterProfiler, using genes with an adjusted p value < 0.05, and log2 fold change greater than 0.4[91]. Enriched terms were determined using enrichGO with default parameters, including the hypergeometric test and Benjamini-Hochberg correction for multiple testing. Exact p values for Gene Ontology analysis are provided in Supplementary Data 4.

Quantification and statistical analysis

Statistical evaluation was performed using a Student's two-tailed t test between two groups and a one-way ANOVA followed by a post hoc test

between more than two groups. Two-way ANOVA with post hoc tests was conducted when more than two groups and variables were compared. Correction for multiple comparisons was conducted. Statistical tests and graph visualization were performed using GraphPad Prism v10, except for the scRNA-seq data analysis, which was visualized and analyzed using R. The exact packages and parameters of the transcriptomic analysis are detailed in the section detailing the scRNA-seq experiments. The number of independent experimental replications and the statistical test used are reported in the figure legends. Data is presented using a box plot where the whiskers indicate the maximum and minimum values, or bar plots where the data is presented as mean ± SEM. For all statistical tests, p-value < 0.05 was considered statistically significant. Unless otherwise indicated, the significance level is indicated as follows: *p < 0.05, **p < 0.01, ***p < 0.001. The exact $p$values are reported in the **Source Data** and the **Supplementary Data files**.

Reporting summary
Further information on research design is available in the Nature Portfolio Reporting Summary linked to this article.

Data availability
The 10X Genomics scRNA-seq data generated in this study have been deposited in GEO under accession code GSE274925. Representative microscopy data are provided for all experiments in the main text and **Supplementary Information**. Raw microscopy files are available from the corresponding author upon reasonable request. **Source data** supporting all graphs and quantifications are provided with this paper. Uncropped blots are included in the Source Data. Source data are provided with this paper.

References
1. Sadoulet-Puccio, H. M. & Kunkel, L. M. Dystrophin and its isoforms. *Brain Pathol.* **6**, 25–35 (1996).
2. Hoffman, E. P., Brown, R. H. & Kunkel, L. M. Dystrophin: The protein product of the Duchenne muscular dystrophy locus. *Cell* **51**, 919–928 (1987).
3. Ibraghimov-Beskrovnaya, O. et al. Primary structure of dystrophin-associated glycoproteins linking dystrophin to the extracellular matrix. *Nature* **355**, 696–702 (1992).
4. Dumont, N. A. et al. Dystrophin expression in muscle stem cells regulates their polarity and asymmetric division. *Nat. Med.* **21**, 1455–1463 (2015).
5. Kodippili, K. & Rudnicki, M. A. Satellite cell contribution to disease pathology in Duchenne muscular dystrophy. *Front Physiol.* **14**, 1180980 (2023).
6. Chang, N. C. et al. The dystrophin glycoprotein complex regulates the epigenetic activation of muscle stem cell commitment. *Cell Stem Cell* **22**, 755–768.e6 (2018).
7. Alexander, M. S. et al. CD82 is a marker for prospective isolation of human muscle satellite cells and is linked to muscular dystrophies. *Cell Stem Cell* **19**, 800–807 (2016).
8. Esper, M. E. et al. Intrinsic muscle stem cell dysfunction contributes to impaired regeneration in the mdx mouse. *J. Cachexia, Sarcopenia Muscle* **16**, e13682 (2025).
9. Houzelstein, D., Lyons, G. E., Chamberlain, J. & Buckingham, M. E. Localization of dystrophin gene transcripts during mouse embryogenesis. *J. Cell Biol.* **119**, 811–821 (1992).
10. Durand, M., Suel, L., Barbet, J. P., Beckmann, J. S. & Fougerousse, F. Sequential expression of genes involved in muscular dystrophies during human development. *Morphologie* **86**, 9–12 (2002).
11. Crone, M. & Mah, J. K. Current and emerging therapies for Duchenne muscular dystrophy. *Curr. Treat. Options Neurol.* **20**, 31 (2018).
12. Farini, A. et al. Inositol 1,4,5-trisphosphate (IP3)-dependent Ca2+ signaling mediates delayed myogenesis in Duchenne muscular dystrophy fetal muscle. *Development* **143**, 658–669 (2016).
13. Nguyen, F., Cherel, Y., Guigand, L., Goubault-Leroux, I. & Wyers, M. Muscle lesions associated with dystrophin deficiency in neonatal golden retriever puppies. *J. Comp. Pathol.* **126**, 100–108 (2002).
14. Bassett, D. I. et al. Dystrophin is required for the formation of stable muscle attachments in the zebrafish embryo. *Development* **130**, 5851–5860 (2003).
15. Merrick, D., Stadler, L. K. J., Larner, D. & Smith, J. Muscular dystrophy begins early in embryonic development deriving from stem cell loss and disrupted skeletal muscle formation. *Dis. Models Mech.* **2**, 374–388 (2009).
16. Pescatori, M. et al. Gene expression profiling in the early phases of DMD: a constant molecular signature characterizes DMD muscle from early postnatal life throughout disease progression. *FASEB J.* **21**, 1210–1226 (2007).
17. Mournetas, V. et al. Myogenesis modelled by human pluripotent stem cells: a multi-omic study of Duchenne myopathy early onset. *J. Cachexia Sarcopenia Muscle* **12**, 209–232 (2021).
18. Mozin, E. et al. Dystrophin deficiency impairs cell junction formation during embryonic myogenesis from pluripotent stem cells. *iScience* **27**, 110242 (2024).
19. McGreevy, J. W., Hakim, C. H., McIntosh, M. A. & Duan, D. Animal models of Duchenne muscular dystrophy: from basic mechanisms to gene therapy. *Dis. Models Mech.* **8**, 195–213 (2015).
20. Bentzinger, C. F., Wang, Y. X. & Rudnicki, M. A. Building Muscle: Molecular Regulation of Myogenesis. *Cold Spring Harb. Perspect. Biol.* **4**, a008342 (2012).
21. Musy, M. et al. A quantitative method for staging mouse embryos based on limb morphometry. *Development* **145**, dev154856 (2018).
22. Resende, T. P., Andrade, R. P. & Palmeirim, I. Timing embryo segmentation: Dynamics and regulatory mechanisms of the vertebrate segmentation clock. *Biomed. Res. Int.* **2014**, 718683 (2014).
23. Kuang, S., Kuroda, K., Le Grand, F. & Rudnicki, M. A. Asymmetric self-renewal and commitment of satellite stem cells in muscle. *Cell* **129**, 999–1010 (2007).
24. Wilson, D. G. S., Tinker, A. & Iskratsch, T. The role of the dystrophin glycoprotein complex in muscle cell mechanotransduction. *Commun. Biol.* **5**, 1–18 (2022).
25. Duddy, W. et al. Muscular dystrophy in the mdx mouse is a severe myopathy compounded by hypotrophy, hypertrophy and hyperplasia. *Skelet. Muscle* **5**, 1–18 (2015).
26. Collins, B. C. et al. Three-dimensional imaging studies in mice identify cellular dynamics of skeletal muscle regeneration. *Dev. Cell* **59**, 1457–1474.e5 (2024).
27. Messina, G. et al. Nfix regulates fetal-specific transcription in developing skeletal muscle. *Cell* **140**, 554–566 (2010).
28. Relaix, F., Rocancourt, D., Mansouri, A. & Buckingham, M. A Pax3/Pax7-dependent population of skeletal muscle progenitor cells. *Nature* **435**, 948–953 (2005).
29. Bjornson, C. R. R. et al. Notch signaling is necessary to maintain quiescence in adult muscle stem cells. *Stem Cells* **30**, 232–242 (2012).
30. Bröhl, D. et al. Colonization of the satellite cell niche by skeletal muscle progenitor cells depends on notch signals. *Dev. Cell* **23**, 469–481 (2012).
31. Baghdadi, M. B. et al. Reciprocal signalling by Notch-Collagen V-CALCR retains muscle stem cells in their niche. *Nature* **557**, 714–718 (2018).
32. Lahmann, I. et al. Oscillations of MyoD and Hes1 proteins regulate the maintenance of activated muscle stem cells. *Genes Dev.* **33**, 524–535 (2019).

33. Machado, L. et al. In situ fixation redefines quiescence and early activation of skeletal muscle stem cells. *Cell Rep.* **21**, 1982–1993 (2017).

34. Urciuolo, A. et al. Collagen VI regulates satellite cell self-renewal and muscle regeneration. *Nat. Commun.* **4**, 1964 (2013).

35. Rayagiri, S. S. et al. Basal lamina remodeling at the skeletal muscle stem cell niche mediates stem cell self-renewal. *Nat. Commun.* **9**, 1075 (2018).

36. Mourikis, P. et al. A critical requirement for notch signaling in maintenance of the quiescent skeletal muscle stem cell state. *Stem Cells* **30**, 243–252 (2012).

37. Girardi, F. et al. TGFβ signaling curbs cell fusion and muscle regeneration. *Nat. Commun.* **12**, 750 (2021).

38. Yamashita, K. et al. The 8th and 9th tandem spectrin-like repeats of utrophin cooperatively form a functional unit to interact with polarity-regulating kinase PAR-1b. *Biochem. Biophys. Res. Commun.* **391**, 812–817 (2010).

39. Bultje, R. S. et al. Mammalian Par3 regulates progenitor cell asymmetric division via notch signaling in the developing neocortex. *Neuron* **63**, 189–202 (2009).

40. Cayouette, M. & Raff, M. Asymmetric segregation of Numb: A mechanism for neural specification from Drosophila to mammals. *Nat. Neurosci.* **5**, 1265–1269 (2002).

41. Gulino, A., Di Marcotullio, L. & Screpanti, I. The multiple functions of Numb. *Exp. Cell Res.* **316**, 900–906 (2010).

42. McGill, M. A. & McGlade, C. J. Mammalian numb proteins promote Notch1 receptor ubiquitination and degradation of the Notch1 intracellular domain. *J. Biol. Chem.* **278**, 23196–23203 (2003).

43. Conboy, I. M. & Rando, T. A. The regulation of Notch signaling controls satellite cell activation and cell fate determination in postnatal myogenesis. *Dev. Cell* **3**, 397–409 (2002).

44. Holowacz, T., Zeng, L. & Lassar, A. B. Asymmetric localization of numb in the chick somite and the influence of myogenic signals. *Dev. Dyn.* **235**, 633–645 (2006).

45. Shinin, V., Gayraud-Morel, B., Gomès, D. & Tajbakhsh, S. Asymmetric division and cosegregation of template DNA strands in adult muscle satellite cells. *Nat. Cell Biol.* **8**, 677–687 (2006).

46. Jory, A. et al. Numb promotes an increase in skeletal muscle progenitor cells in the embryonic somite. *Stem Cells* **27**, 2769–2780 (2009).

47. Chien, C., Wang, S., Rothenberg, M., Jan, L. Y. & Jan, Y. N. Numb-associated kinase interacts with the phosphotyrosine binding domain of numb and antagonizes the function of numb in vivo. *Mol. Cell. Biol.* **18**, 598 (1998).

48. Huang, C., Ji, C. & Wang, J. Current thoughts on cellular functions of numb-associated kinases. *Mol. Biol. Rep.* **50**, 4645–4652 (2023).

49. Sorensen, E. B. & Conner, S. D. AAK1 regulates numb function at an early step in clathrin-mediated endocytosis. *Traffic* **9**, 1791–1800 (2008).

50. Gupta-Rossi, N. et al. The adaptor-associated kinase 1, AAK1, is a positive regulator of the notch pathway. *J. Biol. Chem.* **286**, 18720–18730 (2011).

51. Biressi, S. et al. Intrinsic phenotypic diversity of embryonic and fetal myoblasts is revealed by genome-wide gene expression analysis on purified cells. *Dev. Biol.* **304**, 633–651 (2007).

52. Venters, S. J. & Ordahl, C. P. Asymmetric cell divisions are concentrated in the dermomyotome dorsomedial lip during epaxial primary myotome morphogenesis. *Anat. Embryol.* **209**, 449–460 (2005).

53. Ben-Yair, R. & Kalcheim, C. Lineage analysis of the avian dermomyotome sheet reveals the existence of single cells with both dermal and muscle progenitor fates. *Development* **132**, 689–701 (2005).

54. Masuda-Hirata, M. et al. Intracellular polarity protein PAR-1 regulates extracellular laminin assembly by regulating the dystroglycan complex. *Genes Cells* **14**, 835–850 (2009).

55. Belanto, J. J. et al. Microtubule binding distinguishes dystrophin from utrophin. *Proc. Natl. Acad. Sci. USA* **111**, 5723–5728 (2014).

56. Massouridès, E. et al. Dp412e: a novel human embryonic dystrophin isoform induced by BMP4 in early differentiated cells. *Skelet. Muscle* **5**, 40 (2015).

57. Qiu, C. et al. Systematic reconstruction of cellular trajectories across mouse embryogenesis. *Nat. Genet* **54**, 328–341 (2022).

58. Molina, T., Fabre, P. & Dumont, N. A. Fibro-adipogenic progenitors in skeletal muscle homeostasis, regeneration and diseases. *Open Biol.* **11**, 210110 (2021).

59. Fung, C. W. et al. Cell fate determining molecular switches and signaling pathways in Pax7-expressing somitic mesoderm. *Cell Discov.* **8**, 1–21 (2022).

60. Karuppasamy, M. et al. Conditional Dystrophin ablation in the skeletal muscle and brain causes profound effects on muscle function, neurobehavior, and extracellular matrix pathways. *bioRxiv* 2025.01.30.635777 https://doi.org/10.1101/2025.01.30.635777 (2025).

61. Xi, H. et al. A human skeletal muscle atlas identifies the trajectories of stem and progenitor cells across development and from human pluripotent stem cells. *Cell Stem Cell* **27**, 158–176.e10 (2020).

62. Smith, C. A. et al. aPKC-mediated phosphorylation regulates asymmetric membrane localization of the cell fate determinant Numb. *EMBO J.* **26**, 468–480 (2007).

63. Nishimura, T. & Kaibuchi, K. Numb controls integrin endocytosis for directional cell migration with aPKC and PAR-3. *Dev. Cell* **13**, 15–28 (2007).

64. Su, D. et al. SPTAN1/NUMB axis senses cell density to restrain cell growth and oncogenesis through Hippo signaling. *J. Clin. Invest* **133**, e168888 (2023).

65. Lin, S. et al. Brief report: Blockade of Notch signaling in muscle stem cells causes muscular dystrophic phenotype and impaired muscle regeneration. *Stem Cells* **31**, 823–828 (2013).

66. Vieira, N. M. et al. Jagged 1 rescues the Duchenne muscular dystrophy phenotype. *Cell* **163**, 1204 (2015).

67. Sambasivan, R. et al. Distinct regulatory cascades govern extraocular and pharyngeal arch muscle progenitor cell fates. *Dev. Cell* **16**, 810–821 (2009).

68. Prigge, J. R. et al. Nuclear double-fluorescent reporter for in vivo and ex vivo analyses of biological transitions in mouse nuclei. *Mamm Genome* 10.1007/s00335-013-9469–8 https://doi.org/10.1007/s00335-013-9469-8 (2013).

69. Tallquist, M. D., Weismann, K. E., Hellström, M. & Soriano, P. Early myotome specification regulates PDGFA expression and axial skeleton development. *Development* **127**, 5059–5070 (2000).

70. Bowl, M. R. et al. A large scale hearing loss screen reveals an extensive unexplored genetic landscape for auditory dysfunction. *Nat. Commun.* **8**, 886 (2017).

71. Heyne, G. W. et al. A simple and reliable method for early pregnancy detection in inbred mice. *J. Am. Assoc. Lab Anim. Sci.* **54**, 368–371 (2015).

72. McFarlane, L., Truong, V., Palmer, J. S. & Wilhelm, D. Novel PCR assay for determining the genetic sex of mice. *Sex. Dev.* **7**, 207–211 (2013).

73. Esper, M. E., Kodippili, K. & Rudnicki, M. A. Immunofluorescence labeling of skeletal muscle in development, regeneration, and disease. *Methods Mol. Biol.* **2566**, 113–132 (2023).

74. Rouillard, A. D. et al. The harmonizome: a collection of processed datasets gathered to serve and mine knowledge about genes and proteins. *Database* **2016**, baw100 (2016).

75. Rossi, G. et al. Silencing Nfix rescues muscular dystrophy by delaying muscle regeneration. *Nat. Commun.* **8**, 1055 (2017).

76. Brun, C. E. et al. GLI3 regulates muscle stem cell entry into GAlert and self-renewal. *Nat. Commun.* **13**, 3961 (2022).

77. Renier, N. et al. iDISCO: A simple, rapid method to immunolabel large tissue samples for volume imaging. *Cell* **159**, 896–910 (2014).

78. Hao, Y. et al. Integrated analysis of multimodal single-cell data. *Cell* **184**, 3573–3587.e29 (2021).

79. Hao, Y. et al. Dictionary learning for integrative, multimodal and scalable single-cell analysis. *Nat. Biotechnol.* **42**, 293–304 (2024).

80. Germain, P.-L., Lun, A., Garcia Meixide, C., Macnair, W. & Robinson, M. D. Doublet identification in single-cell sequencing data using scDblFinder. *F1000Res* **10**, 979 (2021).

81. Hafemeister, C. & Satija, R. Normalization and variance stabilization of single-cell RNA-seq data using regularized negative binomial regression. *Genome Biol.* **20**, 296 (2019).

82. Choudhary, S. & Satija, R. Comparison and evaluation of statistical error models for scRNA-seq. *Genome Biol.* **23**, 27 (2022).

83. Kolberg, L. et al. g:Profiler—interoperable web service for functional enrichment analysis and gene identifier mapping (2023 update). *Nucleic Acids Res.* **51**, W207–W212 (2023).

84. Zhou, Y. et al. Metascape provides a biologist-oriented resource for the analysis of systems-level datasets. *Nat. Commun.* **10**, 1523 (2019).

85. Greenbaum, M. P., Iwamori, N., Agno, J. E. & Matzuk, M. M. Mouse TEX14 is required for embryonic germ cell intercellular bridges but not female fertility. *Biol. Reprod.* **80**, 449–457 (2009).

86. Aloisio, G. M. et al. PAX7 expression defines germline stem cells in the adult testis. *J. Clin. Invest* **124**, 3929–3944 (2014).

87. Blanco-Carmona, E. Generating publication ready visualizations for Single Cell transcriptomics using SCpubr. 2022.02.28.482303 Preprint at https://doi.org/10.1101/2022.02.28.482303 (2022).

88. Marsh, S., Salmon, M. & Hoffman, P. scCustomize: Custom visualizations & functions for streamlined analyses of single cell sequencing. Zenodo https://doi.org/10.5281/zenodo.10724532 (2024).

89. Ashburner, M. et al. Gene Ontology: tool for the unification of biology. *Nat. Genet* **25**, 25–29 (2000).

90. The Gene Ontology Consortium et al. The Gene Ontology knowledgebase in 2023. *Genetics* **224**, iyad031 (2023).

91. Wu, T. et al. clusterProfiler 4.0: A universal enrichment tool for interpreting omics data. *Innovation* **2**, 100141 (2021).

Acknowledgements

Author contributions

M.E.E. and M.A.R. conceived the study, designed the experiments and wrote the manuscript. M.E.E. and A.Y.T.L. performed the experiments and analyzed the data. M.E.E., A.Y.T.L., and D.B. designed and conducted the timed mating experiments. M.E.E. analyzed the transcriptomic data. M.A.R. provided guidance, financial support, and resources.

Competing interests

M.A.R. is the Founding Scientist and Chief Discovery Officer of Satellos Bioscience and receives consulting remuneration, and holds stocks and options. The remaining authors declare no conflict of interest.

Additional information

Supplementary information The online version contains supplementary material available at https://doi.org/10.1038/s41467-025-64999-3.

Correspondence and requests for materials should be addressed to Michael A. Rudnicki.

Peer review information *Nature Communications* thanks Giulio Cossu, and the other anonymous, reviewer(s) for their contribution to the peer review of this work. A peer review file is available.

Reprints and permissions information is available at http://www.nature.com/reprints

Publisher's note Springer Nature remains neutral with regard to jurisdictional claims in published maps and institutional affiliations.